

MULTI-BAND OPTICAL AND NEAR-INFRARED PROPERTIES OF FAINT SUBMILLIMETER GALAXIES WITH SERENDIPITOUS ALMA DETECTIONS

PALLAVI PATIL,^{1,2,*} KRISTINA NYLAND,² MARK LACY,² DUNCAN FARRAH,^{3,4} JOSÉ AFONSO,^{5,6} WAYNE BARKHOUSE,⁷ AND JASON SURACE⁸

¹*Department of Astronomy, University of Virginia, 530 McCormick Road, Charlottesville, VA 22903, USA*

²*National Radio Astronomy Observatory, 520 Edgemont Road, Charlottesville, VA 22903, USA*

³*Department of Physics and Astronomy, University of Hawaii, 2505 Correa Road, Honolulu, HI 96822, USA*

⁴*Institute for Astronomy, 2680 Woodlawn Drive, University of Hawaii, Honolulu, HI 96822, USA*

⁵*Instituto de Astrofísica e Ciências do Espaço, Universidade de Lisboa, OAL, Tapada da Ajuda, PT1349-018 Lisboa, Portugal*

⁶*Departamento de Física, Faculdade de Ciências, Universidade de Lisboa, Edifício C8, Campo Grande, PT1749-016 Lisbon, Portugal*

⁷*Department of Physics and Astrophysics, University of North Dakota, Grand Forks, ND 58202-7129, USA*

⁸*California Institute of Technology, 1200 E. California Boulevard, Pasadena, CA 91125, USA*

ABSTRACT

We present a catalog of 26 faint submillimeter galaxies (SMGs) in the XMM-LSS field identified by cross-matching serendipitously detected sources in archival ALMA Band 6 and 7 data with multi-band near-infrared (NIR) and optical data from the *Spitzer* Extragalactic Representative Volume Survey, the VISTA Deep Extragalactic Survey, the Canada-France-Hawaii Telescope Legacy Large Survey, and the Hyper Suprime-Cam Subaru Strategic Program. Of the 26 SMGs in our sample, 15 are identified here for the first time. The majority of the sources in our sample (16/26) have faint submm fluxes ($0.1 \text{ mJy} < S_{1 \text{ mm}} < 1 \text{ mJy}$). In addition to the 26 SMGs with multi-band optical and NIR detections, there are 60 highly-reliable ($> 5\sigma$) ALMA sources with no counterpart in any other band down to an IRAC [4.5] *AB* magnitude of ≈ 23.7 . To further characterize the 26 galaxies with both ALMA and optical/NIR counterparts, we provide 13-band forced photometry for the entire catalog using the *Tractor* and calculate photometric redshifts and rest-frame colors. The median redshift of our sample is $\langle z \rangle = 2.66$. We find that our sample galaxies have bluer colors compared to bright SMGs, and the UVJ color plot indicates that their colors are consistent with main sequence star-forming galaxies. Our results provide new insights into the nature of the faint population of SMGs, and also highlight opportunities for galaxy evolution studies based on archival ALMA data.

Keywords: galaxies:evolution–galaxies:star formation–submillimeter:galaxies–galaxies:photometry–galaxies:high-redshift

1. INTRODUCTION

Dusty Star-Forming Galaxies (DSFGs) are a class of galaxies enshrouded in dust that have star formation rates of at least a few tens of solar masses per year (Casey et al. 2014). A characteristic feature of this class is the bright dust emission at Far-infrared (FIR) wavelengths, which is the re-radiated optical/ultra-violet light from star-forming regions. Their discovery became possible by the advances in IR instruments during the 1980s-1990s, and the *Infra-Red Astronomical Satellite* (IRAS) allowed a large number of detections of Luminous and Ultraluminous Infrared Galaxies (LIRGs and ULIRGs). Furthermore, the Cosmic Background Explorer (COBE) satellite was the first to measure the Cosmic Infrared Background (CIB) light and establish the overall importance of the DSFG population. The results from COBE showed that the energy density of the CIB emission is comparable to the optical and UV background light (Dole et al. 2006; Hauser et al. 1998). Studies in the late 1990s (Smail et al. 1997; Barger et al. 1998; Hughes et al. 1998; Blain et al. 2002, and references therein) identified the galaxies responsible for the CIB submm/mm emission. These galaxies, popularly known as Submillimeter Galaxies (SMG; Blain et al. 2002), belong to the more general class of DSFGs.

SMGs are extremely luminous galaxies ($L_{IR} > 10^{12} L_{\odot}$) with star formation rates up to $1000 M_{\odot} \text{ yr}^{-1}$ (Ivison et al. 1998; Smail et al. 2002; Chapman et al. 2004; Barger et al. 2012; Swinbank et al. 2014; Simpson et al. 2017; Michałowski et al. 2017). They are most likely undergoing a merger (Engel et al. 2010; Ivison et al. 2012; Alaghband-Zadeh et al. 2012; Fu et al. 2013; Chen et al. 2015; Oteo et al. 2016), and have a median redshift, $\langle z \rangle \sim 2-3$ (Chapman et al. 2002, 2005; Wardlow et al. 2011; Simpson et al. 2014; Miettinen et al. 2015; Chen et al. 2016a). Although early studies of SMGs only utilized observation windows at $850 \mu\text{m}$ and 1.1 mm due to atmospheric transmission, the negative k -correction helped to probe SMGs up to high redshift ($z \sim 5$). For a given luminosity, the dimming of the flux with increasing redshift is balanced by the shifting of the peak of the Spectral Energy Distribution (SED) into the observing window (Franceschini et al. 1991; Blain et al. 2002; See Fig. 4 in Blain et al. (2002)). Therefore, the flux remains approximately constant for redshifts up to $z \sim 8$.

Single-dish instruments such as the Submillimetre Common User Bolometer Array (SCUBA; e.g. Smail et al. 1997; Hughes et al. 1998; Barger et al. 1998) on the James Clark Maxwell Telescope (JCMT), AzTEC (Ezawa et al. 2004; Perera et al. 2008; Austermann et al. 2010; Aretxaga et al. 2011; Scott et al. 2010, 2012) on the Atacama Submillimeter Telescope Experiment (ASTE), the Large Apex Bolometer Camera (LABOCA) on the Atacama Pathfinder Experiment (APEX) (Siringo et al. 2009; Weiß et al. 2009), Bolocam on the Caltech Submillimeter Observatory (CSO) (Laurent et al.

2005), the Max Planck Millimeter Bolometer (MAMBO; Greve et al. 2004; Bertoldi et al. 2007) on the IRAM 30-meter telescope, and SCUBA-2 on JCMT (Chen et al. 2013a; Casey et al. 2013; Geach et al. 2013, 2017) identified a significant number of SMGs. However, large beam sizes ($15''$ for SCUBA at $850 \mu\text{m}$ and $11''$ for MAMBO-1 at 1.2 mm) prevented accurate multi-wavelength counterpart identification. A few indirect techniques were used to identify multi-wavelength counterparts, such as using the radio-FIR correlation to find targets in radio interferometric observations (Ivison et al. 2007), $24 \mu\text{m}$ MIPS observations from *Spitzer* (e.g. Pope et al. 2006), and assigning probabilities to the possible optical/NIR counterparts (e.g. Ivison et al. 2002; Dunlop et al. 2004; Chapin et al. 2011; Smith et al. 2011; Kim et al. 2012; Alberts et al. 2013, Biggs et al. 2011). These techniques have limitations as not all counterparts can be accurately identified due to large beam sizes of single dish telescopes. Therefore, interferometric observation is required to obtain a bias-free sample of submm sources with sub-arcsecond positional accuracy.

Number count studies revealed that a significant population was missed by the single dish as well as space-based observations at submm and mm wavelengths (Lagache et al. 2005). On the other hand, most of the population contributing to the CIB at wavelengths less than $200 \mu\text{m}$ was already identified, and found to reside at $z \sim 1$ (Viero et al. 2013). Number counts as well as models, showed that the redshift of the dominant contributor to the CIB increases with increasing wavelength (Lagache et al. 2005). This indicates the need for high sensitivity and finer spatial resolution surveys. During the pre-Atacama Large Millimeter Array (ALMA) era, 1.1 mm surveys were mainly conducted with AzTEC (Perera et al. 2008; Scott et al. 2012; Hatsukade et al. 2011; Austermann et al. 2010; Scott et al. 2010; Aretxaga et al. 2011) and about $10 - 20\%$ of the CIB was resolved (Hatsukade et al. 2011; Scott et al. 2010). In contrast, $850/870 \mu\text{m}$ surveys using SCUBA, the LABOCA has resolved up to 50% of the CIB (Blain et al. 1999; Coppin et al. 2006; Weiß et al. 2009)¹. The high confusion limit limited the detection threshold to $\sim 1-2 \text{ mJy}$ at $850 \mu\text{m}$. Studies of gravitationally-lensed SMGs allowed to probe the faint population (Hsu et al. 2016; Chen et al. 2013b,a; Smail et al. 1997; Cowie et al. 2002; Knudsen et al. 2008; Johansson et al. 2011; Chen et al. 2014). However, these studies were limited by small number statistics and uncertainties in the lensing models for the clusters. In summary, all of the previous results have shown that the major contributors of the CIB at $850 \mu\text{m}$ and 1.1 mm have flux densities fainter than 1 mJy . Such galaxies would

¹ We have provided only a selected number of references here. Refer to Section 3 in Casey et al. (2014) for a complete list.

correspond to normal galaxies, or LIRGs (with luminosities $L < 10^{12} L_{\odot}$).

It is now possible to study this fainter population, the so-called faint SMGs, as ALMA provides sub-arcsecond resolution and high sensitivity at submm and mm wavelengths. However, the small field of view of ALMA makes large surveys challenging. Several groups have tried different approaches to optimize ALMA's resources and search for the faint population. One approach is to look for serendipitous detections using archival observations obtained for other scientific goals (Hatsukade et al. 2013; Ono et al. 2014; Carniani et al. 2015; Fujimoto et al. 2016; Oteo et al. 2016). Another approach is to observe a contiguous field using ALMA (Dunlop et al. 2017; Kohno et al. 2016; González-López et al. 2017; Franco et al. 2018).

A third approach made use of the available deep optical-NIR surveys to develop a triple color selection technique for identification faint galaxies (Chen et al. 2016a). These pilot studies are attempting to address the contribution of faint SMGs to the CIB, their multi-wavelength counterparts, and their role in shaping galaxy formation. The number count studies revealed that faint SMGs contribute significantly to the extragalactic background light (EBL) at 1.1 mm. Fujimoto et al. (2016) found that the contribution of faint SMGs ($0.02 \text{ mJy} < S_{1.2 \text{ mm}} < 1 \text{ mJy}$) can account for all of the CIB at 1.2 mm. If we assume a median redshift, $z \sim 2$, the IR luminosities of faint SMGs are expected to be in the range $10^{11-12} L_{\odot}$ (Chen et al. 2016a). Therefore, this population bridges the gap between extreme star-forming galaxies (bright SMGs) and optical-color selected galaxies with moderate star-formation rates, e.g., Lyman Break Galaxies (LBGs)² and star forming BzK galaxies (sBzKs)³ (Chen et al. 2016a).

Based on optical-NIR color-color plots, the faint SMGs from Fujimoto et al. (2016) were found to represent LBG/sBzK galaxies. However, these studies suffer from small number statistics, and very little is known about this newly discovered population. Robust estimates of demographics, such as number counts, the redshift distribution, the contribution to the cosmic star formation rate density (SFRD), the nature of their multi-wavelength counterparts, and the star formation rate distribution are some of the key issues that need to be addressed.

In this paper, we study faint SMGs in the XMM Large Scale Structure (XMM-LSS) field with multi-band optical and infrared survey data that have serendipitous submm counterparts identified in archival ALMA observations. Many of the sources identified in our sample are faint SMGs,

with $\sim 1 \text{ mm}$ fluxes below 1 mJy . We investigate the properties of this cosmologically important galaxy population by performing multi-band forced photometry to obtain photometric redshifts and place constraints on star formation. Our study also highlights the growing opportunities for probing high-redshift galaxy properties and gaining new insights on cosmic assembly by mining the ALMA archive.

In Section 2, we describe our sample selection procedure. Details on our reduction of the archival ALMA data, source finding strategy, multi-band photometric catalog construction, and photometric redshift determination are given in Section 3. We discuss the multi-wavelength source properties of our sample in Section 4 and provide a summary of our results in Section 5. Throughout this study we adopt a Λ CDM cosmology with $\Omega_M = 0.3$, $\Omega_{\Lambda} = 0.7$, and $H_0 = 70 \text{ km s}^{-1} \text{ Mpc}^{-1}$.

2. SAMPLE

2.1. Optical and Infrared Data

Our sample is drawn from the XMM-LSS field. The XMM-LSS field includes abundant multi-band data at optical and infrared wavelengths from a variety of wide-field surveys. Of particular importance is the availability of deep *Spitzer* IRAC observations at 3.6 and $4.5 \mu\text{m}$ from the *Spitzer* Extragalactic Representative Volume Survey (SERVS; Mauduit et al. 2012) and DeepDrill (P.I. Mark Lacy). SERVS is a post-cryogenic IRAC survey of five well-studied astronomical deep fields with a depth of $2 \mu\text{Jy}$ and a total sky footprint of 18 deg^2 . The DeepDrill survey expands upon the sky coverage of SERVS and provides deep IRAC imaging in three of the four predefined Deep Drilling Fields for the Large Synoptic Survey Telescope over an area of 38.4 deg^2 ($\sim 1 \text{ Gpc}^3$ at $z > 2$).

Observations at 3.6 and $4.5 \mu\text{m}$ are crucial for detecting rest-frame optical emission from galaxies at $z > 4$, and, when combined with additional photometry at optical and NIR wavelengths, provide constraints on important galaxy properties such as photometric redshift. The SERVS and DeepDrill observations in the XMM-LSS field are complemented by additional NIR data from the ground-based VISTA Deep Extragalactic Survey (VIDEO; Jarvis et al. 2013) in the Z , Y , J , H , and K_s bands. In the optical, wide-field data are available from the Canada-France-Hawaii Telescope Legacy Survey Wide field 1 (CFHTLS-W1; Gwyn 2012) and multiple tiers from the first data release of the Hyper Suprime-Cam Subaru Strategic Program (HSC; Aihara et al. 2017). We include the NIR data from SERVS/DeepDrill and VIDEO, as well as broad-band optical data from HSC in the *grizy* filter set and data from CFHTLS-W1 in the u band in our analysis. Thus, we have a total of 13 bands available for determining photometric redshifts. We illustrate the sky coverage of these surveys in Figure 1.

² See Steidel et al. (1996) for more on the properties of LBGs.

³ See Daddi et al. (2004) for the formal definition of SBzKs.

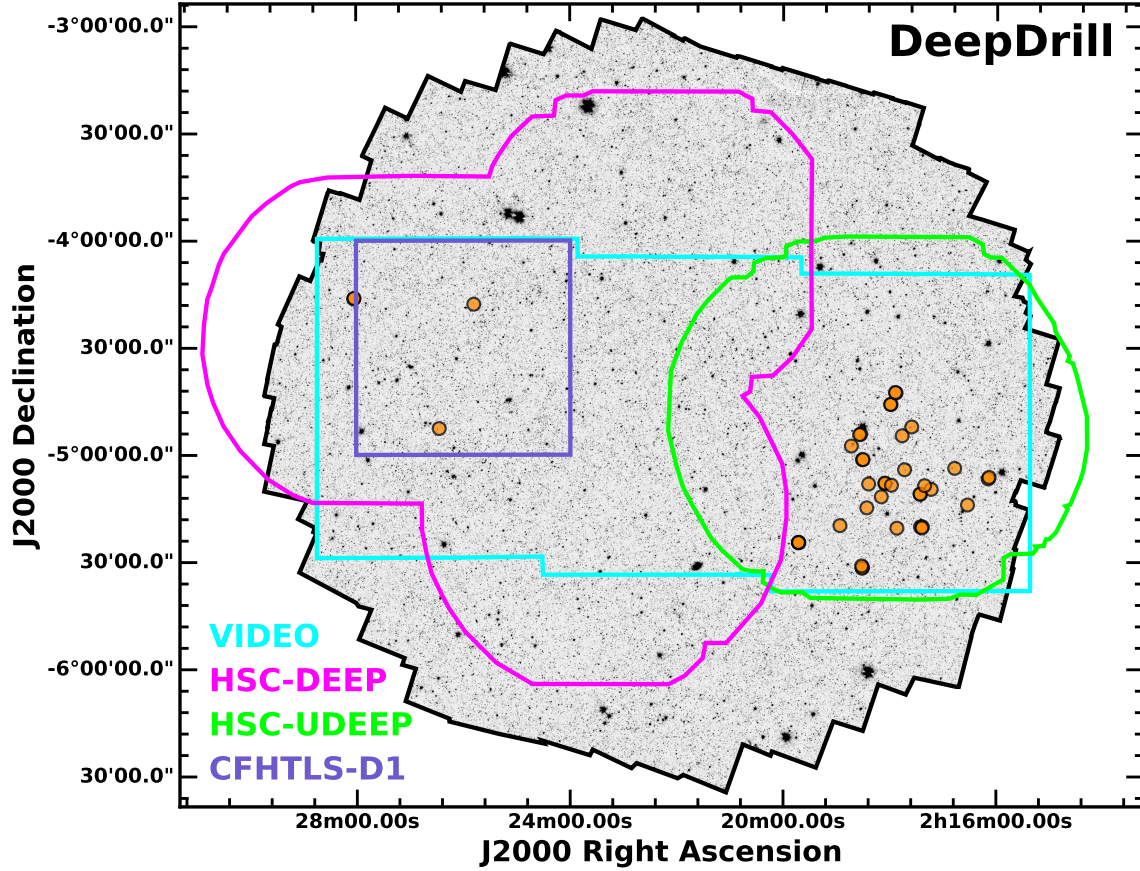


Figure 1. The multi-band coverage by the surveys used in our study in XMM-LSS field. The grayscale image is the DeepDrill $3.6\ \mu\text{m}$ mosaic, the cyan region traces the VIDEO coverage, the green region shows the HSC ultra-deep tier, the magenta region denotes the HSC deep tier, and the purple region shows the CFHT-LS coverage. The orange circles indicate the ALMA sources with optical/NIR counterparts identified in this study.

2.2. Archival ALMA Data

We mined the ALMA archive to search for continuum observations within the XMM-LSS field that were publicly available as of July 2017. We required the following criteria for selecting the archival ALMA data: 1) observations performed in Band 6 (211 – 275 GHz) or Band 7 (275 – 370 GHz), 2) a source integration time longer than 150 seconds to ensure sufficient sensitivity to the inherently faint SMG population, and 3) an angular resolution of $\theta_{\text{FWHM}} > 0.4''$ to ensure adequate surface brightness sensitivity. After evaluating the central depths for all the available programs making the resolution cut, we found that our integration time criterion leads to a maximum 1σ rms noise of $150\ \mu\text{Jy beam}^{-1}$ in Band 6 and $300\ \mu\text{Jy beam}^{-1}$ in Band 7, respectively. Given the nature of our source search, the source depth is variable⁴ and therefore, finding a complete

census of faint SMG is not a primary goal of our search in this paper. We aim to find as many faint galaxies as we can to build up a large sample of the faint population having comprehensive multiwavelength coverage. Such a sample will allow us to conduct detailed studies which will help guide future statistical studies.

Our search identified 75 continuum maps from nine different projects⁵, all but one observed in Band 6. The typical RMS noise levels for Band 6 ($\sim 1.2\ \text{mm}$) and Band 7 ($870\ \mu\text{m}$) are $15\text{--}140\ \mu\text{Jy beam}^{-1}$ and $200\text{--}300\ \mu\text{Jy beam}^{-1}$, respectively. Therefore, we note that the image depth is not uniform throughout our sample. Table 4 summarizes the list

⁴ The source search depth depends on the integration time as well as the distance of the source from the ALMA pointing center. As the noise increases towards the edge of the field of view due to the primary beam re-

sponse, the sensitivity is variable within each pointing. Therefore, specifying the completeness limit would not be meaningful for our study, which aims to explore the properties of the faint SMG population rather than perform a statistically complete analysis.

⁵ The nine public archival ALMA projects were undertaken for entirely different science goals. Brief descriptions of those goals are given in Appendix A.

of ALMA pointings considered for our study. The angular resolutions of the archival data ranged from $0.53''$ to $1.46''$.

3. DATA ANALYSIS

3.1. ALMA

3.1.1. Calibration and Imaging

We reduced the archival ALMA data using the Common Astronomy Software Applications (CASA; McMullin et al. 2007) package. We ran the calibration scripts that are provided along with the raw data from the ALMA archive. The calibration scripts include a-priori flagging, bandpass calibration, flux calibration and gain calibration. The calibrated products were examined for further flagging in the uv-plane as well as image plane. We found that the provided script had flagged most of the bad data and very little additional flagging was required.

We used the CLEAN task to form and deconvolve images with the recommended parameters provided by the ALMA observatory. Specifically, CLEAN was run in multi-frequency synthesis (MFS) mode with $n_{\text{terms}} = 1$. The weighting was either Natural or Briggs weighting with a robust parameter of 0.5, and was determined on a case by case basis. Maps with bright targets were self calibrated (using one round of phase-only self calibration) and re-imaged.

3.1.2. Source Extraction

The Python Blob Detector and Source Finder (PyBDSF) tool was used to extract sources from the ALMA maps (Mohan & Rafferty 2015). Continuum maps without primary beam corrections were used to search for sources. The algorithm looks for image pixels above a specified threshold (here we used $\text{threshpix} = 3.0$). Contiguous pixels above the threshold with a minimum size of $1/3$ of the synthesized beam are formed into a single island. An island is considered a valid source if a single or multiple component Gaussian fit is successful.

We have found that PyBDSF works well with the default parameters. However, we set the pixel threshold parameter to 3.5σ instead of 5σ , as the default threshold was too conservative to probe the fainter population. By lowering the threshold, we are increasing the contamination, but prior source position information from the multi-wavelength optical/infrared data will eliminate most of the spurious sources. The preliminary catalog contains all extracted sources, including the science targets of the proposed observations. We have also removed the sources lying at a distance larger than the radius where the primary beam sensitivity drops to 10% of its maximum, and four strongly lensed galaxies that were the targets of some of the original observations. Although PyBDSF provides estimates of several parameters; total and peak flux densities, convolved and deconvolved source sizes, and uncertainties on each parameter, we chose only to use

it to identify ALMA source position. Those source positions were then cross-matched with the multi-band optical/infrared data (see Section 3.2).

In order to avoid known issues with flux overestimation of faint sources with PyBDSF (Hopkins et al. 2015), we used the JMFIT task from the Astronomical Image Processing Software (AIPS) to measure source fluxes and their uncertainties. For each ALMA source, we used JMFIT to fit a two-dimensional, single-component Gaussian at the position from our source extraction with PyBDSF. All JMFIT measurements were based on the primary-beam-corrected ALMA images. We have tabulated the ALMA fluxes of our sample sources in Table 1.

3.1.3. Detection Threshold

Some spurious detections are likely to contaminate the source catalog, assuming pure Gaussian-like noise. Therefore, it is necessary to determine the signal-to-noise ratio (SNR) cutoff at which an optimal compromise is made between minimizing the number of spurious sources and maintaining a reasonable level of completeness for faint objects. One way to quantify the level of spurious source contamination is to perform a negative peak analysis (Fujimoto et al. 2016; Hatsukade et al. 2013; Ono et al. 2014; Carniani et al. 2015). To accomplish this, we multiplied each ALMA image by -1 and ran PyBDSF using the same input parameters as the ones used in the original source extraction. We then plot separate SNR distributions for all sources extracted from the negative and positive peak analyses.

If a given map only contains noise and no real emission, then the total number of sources in the positive and negative maps would be approximately the same. This will result in a similar source distribution as a function of SNR. However, when real sources are present, we will start to see an excess of positive sources over negative sources above a certain SNR value. The detection threshold for the source catalog can, then, be chosen at a certain value after which the number of positive detections are greater than negative ones. Figure 2 shows the number of sources extracted from both the positive and negative maps from our work. Based on this figure, we selected a detection threshold of 3.9σ for the archival ALMA data. Once this threshold was applied, our ALMA catalog was reduced to 176 objects. We then cross-matched this catalog with the optical-NIR photometry (see Section 3.2) and found 26 faint SMGs with counterparts within a search radius of $1''$.

In order to check the fidelity of our source selection, we performed the same counterpart matching steps for our negative ALMA source catalog and found 7 out of 88 sources with optical-NIR counterparts. Whereas, we found optical-NIR cross-matches for 26 out of 176 sources in the positive source search. Thus, the combination of our detection thresh-

old in the ALMA data and an optical-NIR counterpart leads to a significantly greater level of fidelity compared to the level (50%) that the 3.9σ ALMA detection threshold alone would provide.

In extracting sources from the negative maps, we did find a few targets with multi-Gaussian structures. As we do not expect to see any complex sources, this could be due to image artifacts. Therefore, we excluded sources with such structures from our catalog. We note that we have not estimated the formal completeness of our ALMA catalog, nor are we conducting a number count analysis. Since we are limited by the availability of data in the archive, our sample will naturally be incomplete. In this paper, we focus on investigating the multi-wavelength properties of our sample of faint SMGs.

3.1.4. Comparison with Previous Studies

A few of the ALMA pointings in our sample and that of Fujimoto et al. (2016) overlap, which provides us with an opportunity to compare methodologies, source counts, and source fluxes in the respective samples. In total, 20 ALMA pointings from three different archival programs (ALMA #2011.0.00115.S, #2011.0.00648.S, #2012.1.00934.S) are common with Fujimoto et al. (2016). The source extraction parameters for our study are different from Fujimoto et al. (2016). The authors have selected sources above SNR of 3.4σ within a search radius having primary beam sensitivity of 50% or larger. Whereas, we used 3.9σ as an SNR threshold and a search radius having primary beam sensitivity greater than 10% of its maximum. In our source extraction, we found 26 sources above 3.9σ within those 20 pointings. And Fujimoto et al. (2016) found 14 sources above 3.4σ , out of which 6 sources are above 3.9σ . Those six sources are also detected in our sample. Therefore, source counts of both the studies are consistent when same source extraction parameters are selected. Furthermore, the estimated flux densities also agree within the quoted uncertainties for those six sources.

3.2. Multi-band Forced Photometry

In order to proceed with our photometric redshift and SED analysis, construction of a robust multi-band photometric source catalog is necessary. However, the difference in angular resolution between the *Spitzer* IRAC ($\sim 2''$) and ground-based optical/NIR survey data ($\lesssim 1''$), coupled with the crowded nature of these observations, make the IRAC data prone to issues with source blending. This is problematic for accurate source cross-identification between bands and reliable multi-band photometry.

Recently, Nyland et al. (2017) demonstrated a means of mitigating many of the issues inherent to mixed-resolution optical/NIR datasets using a “forced photometry” approach based on the *Tractor* imaging modeling code (Lang et al. 2016). This code uses prior information on source position

and surface brightness profile from a high-resolution, “fiducial” band, along with image calibration parameters including the point spread function (PSF), to model the source flux in lower-resolution bands. After applying the *Tractor* to a one square degree test region of the XMM-LSS field, Nyland et al. (2017) found a number of improvements in the resulting multi-band forced photometry compared to traditional position-matched source catalogs. In particular, they found that the *Tractor* forced photometry decreased susceptibility to blending issues, led to more reliable source cross-matching between bands, identified a larger number of candidate high-redshift ($z > 5$) objects, and produced more accurate photometric redshifts when compared to available spectroscopic redshift data.

We have adopted a strategy similar to that described in Nyland et al. (2017) in constructing the optical/NIR source catalog used for determining photometric redshifts of the ALMA sources in our study. This strategy requires an initial, position-matched input catalog that is constructed by cross-matching the positions of the ALMA sources with positions from VIDEO⁶ using a search radius of $1''$. Thus, each source in this “VIDEO-selected” input catalog has a detection in the VIDEO catalog in at least one band.

In addition, a “fiducial” VIDEO band is selected for each source that is used for determining the source surface brightness profile model to be applied during the *Tractor* forced photometry. We preferentially select the VIDEO *Ks*-band to be the fiducial band, but if the source is not detected at *Ks*-band, we set the fiducial VIDEO band to the next closest filter in wavelength to the IRAC $3.6\ \mu\text{m}$ band that has a detection reported in the VIDEO source catalog. We note that of 26 ALMA sources with optical-NIR counterparts in our catalog, 23 reside in the UltraDeep tier of HSC (5σ *i*-band depth ~ 27.2 mag) and 3 sources reside in the Deep HSC tier (5σ *i*-band depth ~ 26.5 mag).

For each source in our VIDEO-selected input catalog, we extracted a cutout of the image in each of the 13 bands in our analysis with a half-width of $10''$. To account for spatial variations in the image properties, we measured the sky (RMS) noise and the median background sky level in each image cutout using iterative sigma clipping with Photutils⁷. We then fit the source fluxes using the *Tractor*, which convolves the source surface brightness profile model with the image PSF and uses a maximum likelihood method to optimize the flux of each source in each band, holding the source position, shape, and image calibration properties fixed. We provide the resulting *Tractor* catalog of the forced photometry in Table 2. We also compare the photometry using the

⁶ VIDEO source catalogs and images were obtained from the fifth data release available at <http://horus.roe.ac.uk/vsa/>.

⁷ <http://photutils.readthedocs.io/en/stable/>

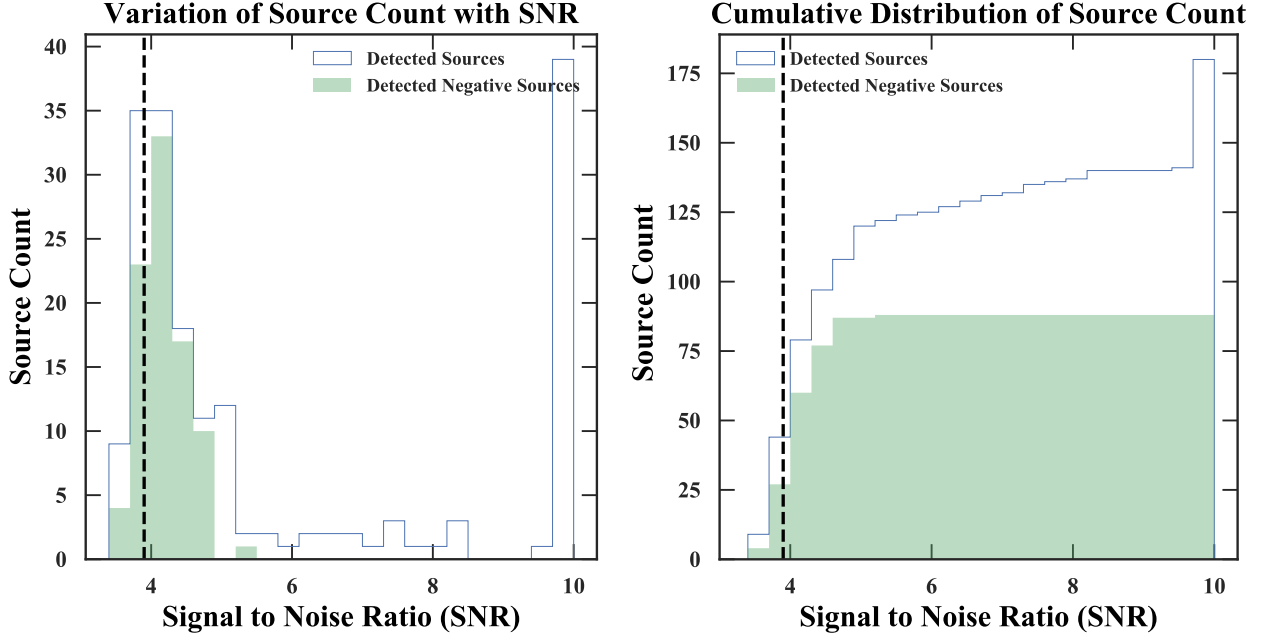


Figure 2. Detection threshold for the archival ALMA images. The left panel shows the differential source count and the right panel shows cumulative source count. This analysis was used to select a detection threshold of 3.9σ for the archival ALMA images.

Tractor with other surveys covering the same field to check consistency of our results. Here we utilize publicly available data release 8 of the UKIDSS-UDS survey. We refer our readers to Appendix B for the detailed discussion.

3.3. Photometric Redshifts

Photometric redshifts were estimated using the Easy and Accurate z_{phot} from Yale (EAZY; Brammer et al. 2008, 2011) software. EAZY performs least square fitting with a linear combination of minimal template sets that can accommodate most of the variations in galaxy properties up to high redshift.

We use a default set SED templates available in EAZY. These templates adequately span the wavelength range to cover the 13-bands used in our analysis ($4.5\mu\text{m}$ to u band). EAZY provides a full probability distribution for the redshift values in the range $0 < z_{\text{phot}} < 6$. We select the photometric redshift of a given source at the value with the highest probability (z_{peak}). The confidence intervals are selected such that the integrated probability distribution is equal to 95%, corresponding to the EAZY output parameters $l95$ and $u95$. Table 1 provides the photometric redshifts along with the 95% confidence limits of our sample.

We illustrate the EAZY photometric redshift fitting results for our sample galaxies in Figure 3. As shown in the green-shaded box in this figure, EAZY provides several diagnostic parameters to quantify the quality of the fit. The fitting results for the entire sample are shown in the appendix Figure 11.

We emphasize that our photometric redshifts are based on multi-band forced photometry using the *Tractor*, a technique that has demonstrated improved photometric redshift accuracy compared to the use of position-matched multi-band photometric catalogs (Nyland et al. 2017). However, given the inherently dusty nature of our sources that may cause deviations in their SEDs that are not well represented by the templates considered in this study, further verification of their redshifts will require a more in-depth SED analysis (to be presented in a forthcoming study) as well as future spectroscopic observations.

The rest frame colors are also evaluated using best fit SED template in EAZY. To estimate colors, we have used filters U , V , and J ⁸. EAZY provides interpolated color indices for each filter of the rest-frame color, such that the colors can be calculated using the following formula; $U - V = -2.5 \times \log(L_U/L_V)$, where L_U and L_V are the calculated U and V -band luminosities, respectively.

3.4. The Final Catalog

We present a catalog of 26 galaxies obtained by cross-matching the ALMA source catalog with optical-NIR observations (Section 2.1). The catalog contains 15 new, serendipitously discovered ALMA detections. From the remaining 11 known sources, nine were detected in the previous stud-

⁸ U and V are standard Bessel filters and the J filter follows the definition of Mauna Kea Consortium defined in Tokunaga et al. (2002).

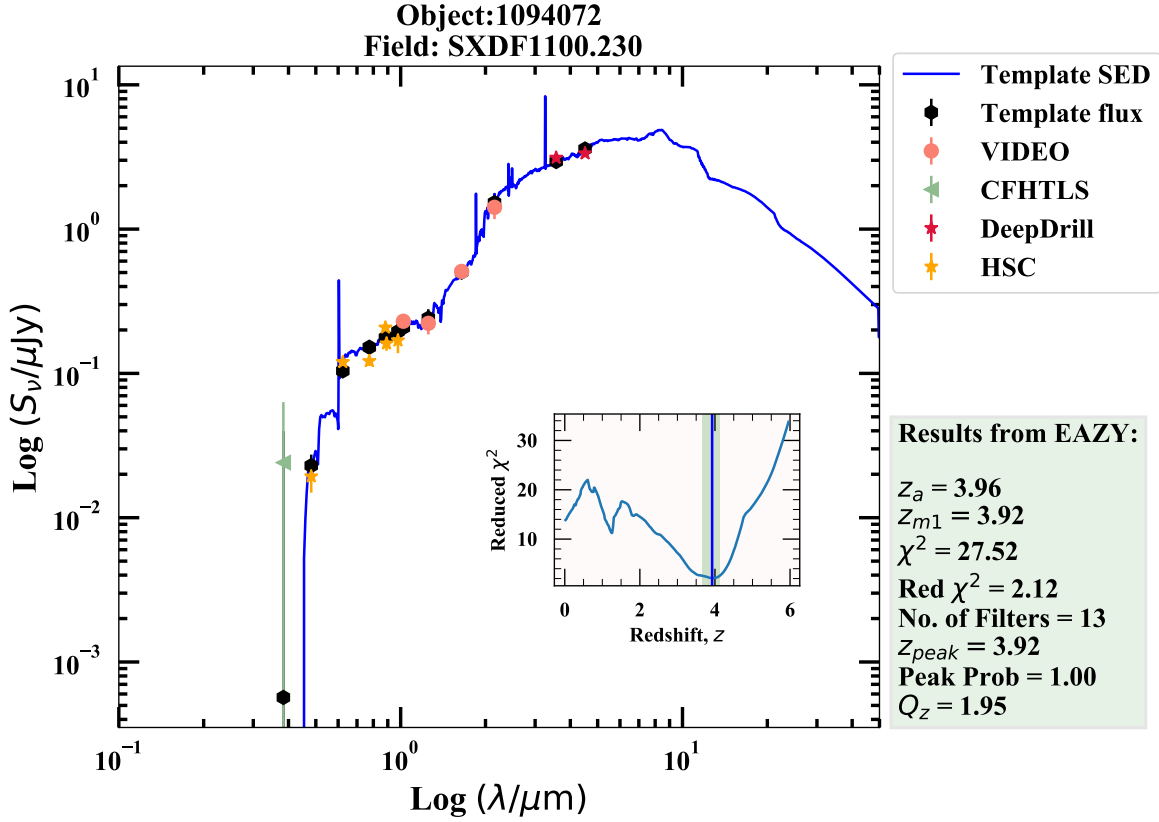


Figure 3. An example of our photometric redshift fitting using EAZY for one of the sources in our sample. The main plot is the observed galaxy SED. Different colored symbols correspond to the observed 13-band photometry obtained using the *Tractor* image modeling code (Section 3.2). Red stars highlight *Spitzer* DeepDrill measurements at 3.6 and 4.5 μm , orange circles denote measurements from the VIDEO survey, the green triangle represents the optical *u*-band data from CFHTLS, and yellow stars mark the optical data points from HSC. The fitted SED template is plotted in blue and the estimated template flux for each filter is shown by the black filled circles. The green box on the right lists key output parameters from EAZY. The inset figure shows the χ^2 distribution of the fit at each redshift bin. The peak of the redshift distribution after applying the prior is shown by the blue vertical line and the light green regions are the 95% confidence intervals of the fit.

ies, and three correspond to a single bright *Herschel* source (Busmann et al. 2015). We explain the properties of all previous detections later in this section. Figure 9 shows the four-band (ALMA Band 6 or 7, *Spitzer* 3.6 and 4.5 μm , and VIDEO K_s) snapshots of the entire catalog. Table 1 summarizes the ALMA properties of our sample sources, our photometric redshifts, and any previously published redshift information. Throughout this paper, we will be identifying sources by their IAU names given in column 1 of Table 1.

Nearly half of our targets (11/26) were previously detected in the SIRTf Wide-area Infra Red Extragalactic Survey (SWIRE; Lonsdale et al. 2004) and have published photometric redshifts using the five-band SWIRE observations (Rowan-Robinson et al. 2008, 2013). Another study that included a large number of our sample galaxies (13 out of 26) is that of Williams et al. (2009). These authors presented a K -band-selected galaxy catalog combining optical-mid IR photometry from SWIRE, the Ultra Deep Survey (UDS) tier of

the UKIRT Infrared Deep Sky Survey (UKIDSS; Lawrence et al. 2007), and the Subaru-XMM Deep Survey (SXDS; Sekiguchi & SXDS Team 2004; Furusawa et al. 2008). They have used EAZY to estimate photometric redshifts based on $BR'z'JK[3.6\mu\text{m}][4.5\mu\text{m}]$ photometry. Our photometric redshifts are in good agreement with previously published values (when available) within the margin of the uncertainties. We emphasize that the 13-band forced photometry presented here provides redshift estimates that are robust against the effects of source blending in the IRAC bands and utilize a large number of filters compared to the previous studies.

4. DISCUSSION

4.1. Flux and Redshift Distribution

We show the flux distribution of our catalog in Figure 4. 57% of the sources have fluxes fainter than 1 mJy. The bino-

mial uncertainty⁹ for each flux density bin is shown as the red line at the center of each bin. We plot the redshift distribution of the entire sample in Figure 5. Two separate histograms for different frequency bands (blue for Band 6 and red for Band 7) are shown. The median redshifts for bands 6 and 7 are $\langle z \rangle = 2.72$ and 2.57 , respectively. We also compare the median redshift values from our work with other ALMA surveys. Our median redshift falls within the range of redshifts from other recent studies of SMGs.

B  thermin et al. (2015) showed that the median redshift of the sample of dusty galaxies depends significantly on the depth and the observing wavelength of the infrared surveys. They concluded that the median redshift increases with increasing wavelength up to 2 mm due to the negative k -correction. However, increasing the observing depth results in the detections of the lower-redshift, fainter sources. Hence, the observed variation in median values could just be an outcome of the varying depth of the surveys. The 1σ rms level in the ~ 1.1 mm surveys by Aravena et al. (2016) and Dunlop et al. (2017) are $13 \mu\text{Jy beam}^{-1}$ and $30 \mu\text{Jy beam}^{-1}$, respectively. The median redshift values of their samples are also lower compared to the other studies ($\langle z \rangle = 1.6$ and 2.15). The survey by Brisbin et al. (2017) has a shallower depth of $150 \mu\text{Jy}$ and, therefore, a higher median redshift of 2.48 . Continuing the trend, Franco et al. (2018) found a population at a median value of $\langle z \rangle = 2.9$ based on their survey with a sensitivity of $450 \mu\text{Jy}$. In case of our work, the average depths for the Band 6 and 7 are $110 \mu\text{Jy}$ and $300 \mu\text{Jy}$, respectively. As we have only five galaxies in Band 7, we exclude those galaxies from any further analysis involving the median redshift. Even though we find a slightly larger median redshift for a depth shallower than Brisbin et al. (2017), the redshifts and depths are comparable within the margin of errors. Therefore, our redshift distribution is consistent with other studies discussed in this section and the predictions by B  thermin et al. (2015).

4.2. Previously Identified Galaxies

As mentioned before, 11 ALMA detections in our catalog are not new. If these targets are DFSGs and unlensed, we have still included them in our catalog. With the availability of multi-wavelength observations from SERVS and our robust 13-band photometry, we can better understand the nature of the previously identified galaxies and the overall population in general. We provide the references to the previous ALMA detection in Column 11 of Table 1. Four out of 11 galaxies were serendipitously detected in previous ALMA archival mining studies (*J0216-0506*, *J0217-0454*: Fujimoto

et al. 2016; Hatsukade et al. 2015; *J0217-0442*: Fujimoto et al. 2016; *J0217-0508*: Ono et al. 2014).

Six of the 11 known galaxies are detected in the ALMA follow-up programs of the bright DFSGs. However, we still include targets in our analysis both the faint and bright SMGs belong to the same category of dusty galaxies. Also, it would be interesting to observe differences in the multi-wavelength properties of these two classes. Three of the six bright SMGs belong to a single Herschel source (*J0219-0524.63*, *J0219-0524.77*, *J0219-0524.84*; Bussmann et al. 2015). The Herschel source is resolved into multiple components at the ALMA resolution. The alignment and similar mid-IR colors of these three galaxies indicate an overdense region. The ALMA flux densities of these targets are larger than the rest of our sample galaxies, but we will still include them to compare the physical properties. Rest of the three galaxies (*J0217-0508*, *J0217-0445*, *J0217-0504*) are selected from the AzTEC survey. These dusty, $z > 3$ bright SMGs are thought to be the progenitors of low redshift massive ellipticals (Ikarashi et al. 2015). They typically host a compact starburst in their centers, and their luminosities are comparable to nearby ULIRGs.

The remaining galaxy *J0226-0452* from the WMH5 field is a $z \sim 6$ UV-luminous Lyman-break galaxy (Willott et al. 2013). As some of the sources in our sample are part of the original ALMA program, that could lead to potential environmental biases in our results. However, 10 out of 11 galaxies are either faint SMGs or selected from bright SMG surveys. Only one galaxy from our sample is the primary target of the original ALMA program, and no other galaxy has the same redshift as the primary target (where the redshift of the primary target is known). Given the small amount of overlap between the ALMA primary targets and our faint SMGs, we do not believe that our sample is significantly affected by environmental biases.

Spectroscopic redshifts are available for three targets (*J0226-0452*, *J0216-0506*, *J0217-0454*) taken from different studies, and the references are given in the Table 1. Target *J0216-0506* is detected in most of the studies mentioned above, and Seko et al. (2016a) have discussed the spectroscopic redshift and ISM properties of that galaxy. It is a member of the sample of $z \sim 1.4$ star-forming main sequence galaxies. CO emission studies with ALMA have indicated larger molecular gas fractions and gas-to-dust ratios than local galaxies. Banerji et al. (2011) have identified the target *J0217-0454* as Submillimeter Faint Radio Galaxy (SFRG) which are similar to bright SMGs but have hotter dust temperatures. Its spectroscopic redshift ($z = 1.456$) was measured using [OII] 3727 emission line. In all the cases, the spectroscopic redshifts are well within the 95% confidence interval of our photometric redshifts.

⁹ The binomial uncertainty is defined as $\sigma_{n_i} = \sqrt{n_i(1 - n_i/N)}$ where n_i is the number of galaxies in bin i and N is the total number of galaxies.

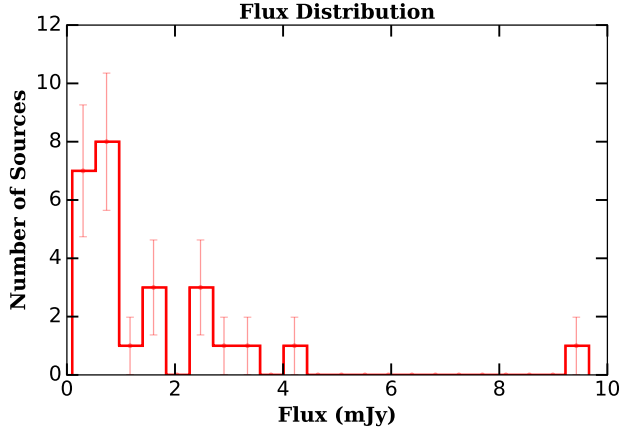


Figure 4. The flux distribution of our sample. The red line at the center of each bin is the binomial uncertainty. There are 15/26 galaxies (57%) with fluxes fainter than 1 mJy. Except for one very bright galaxy ($S \sim 9.5$ mJy), the rest of the bright sample has fluxes ranging from 1 to 5 mJy.

Figure 6 compares the performance of our redshift estimation with archival results. The purpose of this comparison is to conduct a consistency check on the forced photometry technique used in this work. The overall uncertainties on the photo- z estimates are small in most cases. The values are in very good agreement at lower redshifts, $z < 2.5$. However, at higher redshifts, we see an increased scatter in the redshift agreement. This could potentially be due to large uncertainties in the photometric measurements, differences in the filters used for the photo- z estimation, and inherent limitations of the SED templates. Our photometry includes u -band data which is lacking in the previous studies. Also, different methods of source deblending in the *Spitzer* bands could lead to differences in the photometry. This issue can be resolved using spectroscopic data.

4.3. Optical-NIR Triple Color Selection

Chen et al. (2016b) have devised a selection technique to identify bright as well as faint SMGs using a training dataset from the UKIDSS-UDS field. The method is called Optical-Infrared Triple Color selection (OIRTC) and uses three optical-NIR colors: $z - K_s$, $K_s - [3.6]$, and $[3.6] - [4.5]$. The color cuts are defined such that the mean SMG fraction redder than the color threshold is at least 5%. The training sample contains ALMA and 850 μm SCUBA-2 observations of bright SMGs. By combining radio and optical-NIR selection techniques, their identification is about 83% complete. Chen et al. (2016a) have utilized this technique to identify faint SMGs with expected fluxes, $S_{850 \mu\text{m}} < 2$ mJy.

Here, we compare the optical-IR colors of our faint SMG sample with the color selection method described in Chen et al. (2016b). Figure 7 illustrates the OIRTC color selection,

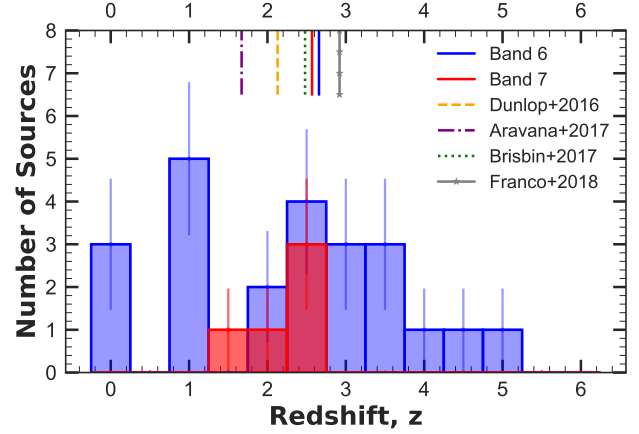


Figure 5. The redshift distribution of the faint SMGs. The photometric redshifts are evaluated using EAZY (Section 3.3). We show separate histograms for the ALMA frequency bands, 6 and 7. A line at the center of the bin shows the binomial uncertainty in each bin. The vertical lines at the top are the median redshifts for our sample as well as other faint SMG samples. Blue and red solid lines show the median values for the Band 6 and 7, respectively. Other studies included in the plot are: Aravena et al. (2016) – Red dash-dotted line; Dunlop et al. (2017) – Orange dashed line; Brisbin et al. (2017) – Green dotted line; Franco et al. (2018) – Silver solid line with star symbols. The average depth for our Band 6 sample is 110 μJy . The median redshift and depth of Band 6 data are consistent with the findings of Béthermin et al. (2015).

where different colored symbols represent our sample along with faint SMG samples of Fujimoto et al. (2016), Hatsukade et al. (2015), Laporte et al. (2017), and Yamaguchi et al. (2016). A comparison with other samples will allow us to evaluate the significance of our results and also to check the consistency between different methods adopted in all of the studies. We see that almost our entire sample occupies the color space outside the selection cuts defined by the OIRTC technique. Furthermore, the galaxies from the comparison samples also lie mostly outside the OIRTC color selection. The light-grey symbols in Figure 7 are the non-SMG field galaxies found within the search radius of all the ALMA pointings used in our study. These field galaxies will allow us to check whether the colors of faint SMGs are systematically redder.

We observe that 75% of faint SMGs satisfy the $z - K_s$ color criterion of having redder colors than the OIRTC $z - K_s$ color criterion. Whereas only 47% and 18% of the faint SMG population satisfy the OIRTC $[3.6] \mu\text{m} - [4.5] \mu\text{m}$ and $K_s - [3.6] \mu\text{m}$ color criteria, respectively. Laporte et al. (2017) and Cowie et al. (2018) have also analyzed the OIRTC criteria for their sample sources. Both the studies found that majority of their samples do not satisfy the OIRTC $K_s - [3.6] \mu\text{m}$ cut. A few factors could be responsible for the differences. The primary extrinsic factor is the varia-

Table 1. ALMA Source Catalog

Source	IAU ID	Field	RA	Dec.	λ_{obs}	$S_{\lambda_{obs}}$	z_{phot}	$z_{archival}$	Ref.	ALMA Ref.
			(J2000)	(J2000)	(mm)	(mJy)				
(1)	(2)	(3)	(4)	(5)	(6)	(7)	(8)	(9)	(10)	(11)
191313	J0226-0452	WMH5	02h26m27.00s	-04d52m38.38s	1.14	0.18 ± 0.04	$4.87^{+1.07}_{-0.26}$	6.068^{\dagger}	4	a
309436	J0225-0417	XMMF6	02h25m48.03s	-04d17m48.96s	0.87	1.33 ± 0.53	$2.77^{+0.14}_{-0.25}$
315617	J0228-0416	CLM1	02h28m02.58s	-04d16m06.99s	1.16	0.17 ± 0.03	$0.29^{+0.26}_{-0.09}$
477360	J0219-0524.63	XMMF16	02h19m42.63s	-05d24m37.07s	0.87	9.66 ± 1.22	$1.75^{+0.16}_{-0.11}$	2.048	1	b
814024	J0219-0524.52	XMMF16	02h19m42.52s	-05d24m41.27s	0.87	2.61 ± 0.50	$2.49^{+0.46}_{-0.42}$
842544	J0219-0524.77	XMMF16	02h19m42.77s	-05d24m36.43s	0.87	2.81 ± 0.50	$2.57^{+0.22}_{-0.24}$	1.489	1	b
911805	J0219-0524.84	XMMF16	02h19m42.84s	-05d24m35.11s	0.87	2.69 ± 0.49	$2.97^{+0.12}_{-0.12}$	1.489	1	b
932297	J0217-0520	SXDF1100.277	02h17m23.50s	-05d20m08.62s	1.13	2.28 ± 0.41	$3.62^{+0.12}_{-0.12}$
935442	J0218-0519	SXDF.220GHZ	02h18m56.10s	-05d19m51.00s	1.33	0.10 ± 0.03	$1.38^{+0.09}_{-0.12}$	$1.48^{+0.10}_{-0.07}$	1,2	...
971686	J0217-0511	UDS16	02h17m25.72s	-05d11m03.17s	1.24	0.10 ± 0.03	$2.73^{+0.20}_{-0.23}$	$0.27^{+2.66}_{-0.05}$	2	...
978351	J0217-0510	UDS16	02h17m26.10s	-05d10m58.20s	1.24	0.95 ± 0.12	$2.12^{+0.14}_{-0.34}$	$1.55^{+0.20}_{-0.07}$	1,2	...
987090	J0217-0508	SXDF1100.027	02h17m20.95s	-05d08m37.17s	1.13	1.39 ± 0.18	$2.95^{+0.10}_{-0.60}$	$2.80^{+0.48}_{-0.70}$	1,5	c
993676	J0216-0506	SXDS5.28019	02h16m08.51s	-05d06m15.89s	1.27	0.18 ± 0.10	$1.29^{+0.05}_{-0.08}$	1.348^{\dagger}	1,2,6	d,e
998253	J0217-0508	HIMIKO	02h17m58.28s	-05d08m30.64s	1.16	0.59 ± 0.04	$1.14^{+0.11}_{-0.08}$	$1.09^{+0.03}_{-0.04}$	1,2	f
1002990	J0216-0503	SXDF1100.013	02h16m47.10s	-05d03m44.54s	1.13	1.46 ± 0.18	$3.03^{+0.23}_{-2.27}$
1017745	J0218-0501	SXDF1100.039	02h18m30.98s	-05d01m23.22s	1.13	0.49 ± 0.17	$0.42^{+0.10}_{-0.11}$	$0.49^{+0.03}_{-0.03}$	1,2	...
1048801	J0217-0454	SXDS1.59863	02h17m46.28s	-04d54m39.77s	1.23	0.69 ± 0.20	$2.29^{+0.10}_{-1.10}$	1.456^{\dagger}	1,2,3	d,e
1094072	J0217-0445	SXDF1100.230	02h17m59.38s	-04d45m53.13s	1.13	1.54 ± 0.14	$3.92^{+0.20}_{-0.27}$	$3.50^{+0.40}_{-0.18}$	1,2,5	c
1106738	J0217-0442	SXDS2.22198	02h17m53.17s	-04d42m39.61s	1.27	0.44 ± 0.10	$0.03^{+0.04}_{-0.02}$	d
1266981	J0217-0520	SXDF1100.277	02h17m23.95s	-05d20m28.02s	1.13	0.55 ± 0.14	$2.66^{+0.11}_{-0.10}$	$2.54^{+0.43}_{-0.40}$	1	...
1302443	J0218-0501	SXDF1100.039	02h18m30.23s	-05d01m21.19s	1.13	0.84 ± 0.17	$3.21^{+0.39}_{-0.41}$	$2.66^{+0.94}_{-0.73}$	1	...
1302615	J0217-0520	SXDF1100.250	02h17m52.00s	-05d20m32.34s	1.13	0.97 ± 0.14	$3.65^{+0.81}_{-1.20}$	$2.79^{+0.45}_{-1.45}$	1	...
1303410	J0218-0508	SXDF1100.109	02h18m23.99s	-05d08m11.40s	1.13	0.79 ± 0.31	$3.16^{+0.20}_{-0.21}$	$1.91^{+0.61}_{-0.39}$	1	...
1304155	J0217-0452	SXDF1100.063	02h17m35.50s	-04d52m11.79s	1.13	0.62 ± 0.17	$2.59^{+0.44}_{-0.45}$
1307256	J0218-0457	SXDF1100.179	02h18m43.41s	-04d57m33.05s	1.13	0.79 ± 0.14	$5.40^{+0.56}_{-5.38}$
1312163	J0217-0504	SXDF1100.110	02h17m43.58s	-05d04m10.31s	1.13	2.61 ± 0.30	$4.47^{+1.44}_{-1.13}$	$4.98^{+0.72}_{-3.14}$	5	c

NOTE—Column 1: Source name. Column 2: Source name based on the IAU convention. Column 3: Field name indicated in the ALMA archive. Columns 4-5: Source right ascension and declination. The position corresponds to the peak of the Gaussian source fitted using PyBDSF. Column 6: ALMA observing wavelength. Column 7: ALMA integrated flux. Column 8: Photometric redshift estimated using our *Tractor* forced photometry (Table 2). Column 9: Previously published source redshift. Values marked by the \dagger symbol are spectroscopic redshifts; the rest are photometric redshifts. Column 10: References for literature redshifts and previous detections at all wavelengths: (1) Rowan-Robinson et al. (2013); (2) Williams et al. (2009); (3) Banerji et al. (2011); (4) Willott et al. (2013); (5) Ikarashi et al. (2015); (6) Seko et al. (2016a). Column 11: References for previous ALMA detections: (a) Willott et al. (2015); (b) Bussmann et al. (2015); (c) Ikarashi et al. (2015); (d) Fujimoto et al. (2016); (e) Hatsukade et al. (2013); (f) Ono et al. (2014)

\dagger Spectroscopic Redshifts

Table 2. Multi-band Tractor Photometry

Source (1)	F_{Ks} (2)	F_H (3)	F_J (4)	F_Y (5)	F_Z (6)	$F_{u'}$ (7)	F_g (8)	F_r (9)	F_i (10)	F_z (11)	F_y (12)	$F_{3.6\mu m}$ (13)	$F_{4.5\mu m}$ (14)
191313 [†]	0.37 ± 0.06	0.62 ± 0.14	0.35 ± 0.03	0.47 ± 0.02	0.28 ± 0.01	-0.03 ± 0.01	-0.04 ± 0.01	-0.07 ± 0.01	-0.06 ± 0.02	0.54 ± 0.04	0.38 ± 0.08	1.35 ± 0.07	0.81 ± 0.10
309436 [†]	7.43 ± 0.83	6.48 ± 0.22	2.39 ± 0.10	1.38 ± 0.07	1.05 ± 0.05	0.04 ± 0.02	0.28 ± 0.02	0.90 ± 0.03	0.84 ± 0.05	1.06 ± 0.08	1.32 ± 0.14	7.00 ± 0.14	12.92 ± 0.13
315617 [†]	0.51 ± 0.07	0.91 ± 0.16	0.81 ± 0.04	0.78 ± 0.03	0.55 ± 0.02	...	0.01 ± 0.01	0.20 ± 0.01	0.31 ± 0.02	0.42 ± 0.04	0.54 ± 0.07	-0.20 ± 0.07	-0.92 ± 0.10
477360	6.83 ± 0.72	3.05 ± 0.12	1.23 ± 0.07	0.23 ± 0.04	-0.31 ± 0.02	-0.01 ± 0.08	-0.10 ± 0.01	-0.21 ± 0.02	-0.02 ± 0.02	-0.01 ± 0.04	0.36 ± 0.08	13.61 ± 0.06	24.10 ± 0.09
814024	1.77 ± 0.27	0.93 ± 0.06	0.21 ± 0.04	0.05 ± 0.02	0.02 ± 0.01	-0.03 ± 0.04	0.01 ± 0.01	0.03 ± 0.01	0.01 ± 0.01	0.02 ± 0.02	0.10 ± 0.04	5.37 ± 0.08	7.12 ± 0.11
842544	2.20 ± 0.29	1.68 ± 0.07	0.31 ± 0.03	0.18 ± 0.02	0.12 ± 0.01	0.01 ± 0.04	-0.01 ± 0.01	0.09 ± 0.01	0.05 ± 0.01	0.05 ± 0.02	-0.00 ± 0.04	10.84 ± 0.07	15.77 ± 0.09
911805	11.12 ± 1.12	9.23 ± 0.30	3.89 ± 0.14	3.61 ± 0.12	3.04 ± 0.10	0.34 ± 0.10	1.40 ± 0.04	1.95 ± 0.06	2.54 ± 0.08	2.94 ± 0.10	3.04 ± 0.14	24.17 ± 0.07	32.00 ± 0.09
932297	0.71 ± 0.09	0.59 ± 0.06	0.39 ± 0.05	0.51 ± 0.09	0.47 ± 0.02	0.00 ± 0.04	0.15 ± 0.01	0.46 ± 0.02	0.44 ± 0.02	0.52 ± 0.03	0.49 ± 0.04	-0.14 ± 0.07	0.17 ± 0.08
935442	16.62 ± 1.54	10.80 ± 0.33	5.54 ± 0.18	4.02 ± 0.12	1.99 ± 0.06	0.11 ± 0.06	0.31 ± 0.01	0.57 ± 0.02	1.06 ± 0.03	1.83 ± 0.06	3.06 ± 0.11	26.82 ± 0.04	29.01 ± 0.05
971686	0.44 ± 0.07	0.64 ± 0.05	0.35 ± 0.04	0.42 ± 0.07	0.29 ± 0.01	0.05 ± 0.04	0.30 ± 0.01	0.37 ± 0.01	0.31 ± 0.01	0.30 ± 0.02	0.27 ± 0.03	0.61 ± 0.03	1.07 ± 0.05
978351	19.63 ± 1.82	10.49 ± 0.33	4.96 ± 0.17	2.16 ± 0.08	1.16 ± 0.04	0.11 ± 0.09	0.18 ± 0.01	0.44 ± 0.02	0.77 ± 0.03	1.17 ± 0.05	1.86 ± 0.09	39.81 ± 0.04	48.34 ± 0.06
987090	7.04 ± 0.67	3.63 ± 0.12	0.73 ± 0.05	0.29 ± 0.02	0.18 ± 0.01	0.01 ± 0.05	-0.01 ± 0.00	0.01 ± 0.01	0.05 ± 0.01	0.13 ± 0.02	0.22 ± 0.04	15.35 ± 0.04	14.16 ± 0.06
993676	14.72 ± 1.35	11.32 ± 0.35	6.05 ± 0.19	5.67 ± 0.17	3.98 ± 0.12	0.48 ± 0.06	0.83 ± 0.03	1.36 ± 0.04	2.06 ± 0.06	3.79 ± 0.12	4.79 ± 0.15	19.85 ± 0.06	21.56 ± 0.09
998253	20.95 ± 1.93	12.57 ± 0.39	6.75 ± 0.23	5.56 ± 0.17	4.35 ± 0.14	0.48 ± 0.10	0.82 ± 0.03	1.28 ± 0.04	2.21 ± 0.07	4.30 ± 0.13	5.09 ± 0.17	37.95 ± 0.08	35.73 ± 0.08
1002990	-0.06 ± 0.06	0.19 ± 0.04	0.21 ± 0.03	0.01 ± 0.02	0.13 ± 0.03	0.02 ± 0.03	0.06 ± 0.00	0.08 ± 0.01	0.10 ± 0.01	0.15 ± 0.01	0.16 ± 0.03	0.53 ± 0.06	0.32 ± 0.09
1017745	19.10 ± 1.77	16.91 ± 0.52	11.27 ± 0.35	11.30 ± 0.34	9.29 ± 0.28	1.04 ± 0.10	2.00 ± 0.06	4.96 ± 0.15	7.11 ± 0.21	9.10 ± 0.28	10.68 ± 0.33	9.72 ± 0.12	9.64 ± 0.12
1048801	13.33 ± 1.27	7.36 ± 0.24	3.83 ± 0.14	2.19 ± 0.08	1.56 ± 0.05	0.19 ± 0.08	0.47 ± 0.02	0.68 ± 0.02	1.06 ± 0.04	1.62 ± 0.06	1.88 ± 0.08	26.22 ± 0.04	32.26 ± 0.07
1094072	1.42 ± 0.24	0.51 ± 0.05	0.22 ± 0.04	0.23 ± 0.02	0.21 ± 0.01	0.02 ± 0.04	0.02 ± 0.00	0.12 ± 0.01	0.12 ± 0.01	0.16 ± 0.02	0.17 ± 0.03	3.13 ± 0.03	3.35 ± 0.06
1106738	0.75 ± 0.11	1.19 ± 0.25	0.86 ± 0.06	0.99 ± 0.04	0.94 ± 0.03	0.24 ± 0.06	0.68 ± 0.02	0.91 ± 0.03	0.96 ± 0.03	1.01 ± 0.04	1.00 ± 0.07	0.00 ± 0.05	-0.08 ± 0.06
1266981	10.22 ± 1.02	5.58 ± 0.19	0.74 ± 0.09	0.56 ± 0.04	0.23 ± 0.02	0.02 ± 0.07	0.00 ± 0.01	0.07 ± 0.01	0.14 ± 0.02	0.20 ± 0.03	0.41 ± 0.06	21.25 ± 0.05	27.94 ± 0.06
1302443	1.43 ± 0.27	0.57 ± 0.06	0.14 ± 0.05	-0.05 ± 0.03	-0.01 ± 0.02	-0.02 ± 0.04	0.02 ± 0.01	0.04 ± 0.01	0.03 ± 0.01	0.22 ± 0.03	-0.01 ± 0.04	3.96 ± 0.13	6.70 ± 0.16
1302615	1.15 ± 0.27	0.30 ± 0.05	-0.04 ± 0.05	0.05 ± 0.02	-0.11 ± 0.01	-0.01 ± 0.04	0.00 ± 0.01	0.02 ± 0.01	0.01 ± 0.01	0.04 ± 0.02	0.06 ± 0.04	3.34 ± 0.03	4.86 ± 0.05
1303410	1.87 ± 0.28	0.96 ± 0.06	0.31 ± 0.04	0.02 ± 0.02	0.11 ± 0.01	-0.01 ± 0.04	0.00 ± 0.01	-0.00 ± 0.01	0.01 ± 0.01	0.05 ± 0.02	-0.02 ± 0.03	4.82 ± 0.04	5.93 ± 0.07
1304155	1.60 ± 0.28	0.88 ± 0.07	0.16 ± 0.06	0.12 ± 0.04	0.03 ± 0.04	-0.05 ± 0.06	0.01 ± 0.01	0.04 ± 0.01	0.03 ± 0.01	0.01 ± 0.02	0.08 ± 0.04	5.88 ± 0.07	8.44 ± 0.09
1307256	0.61 ± 0.26	-0.14 ± 0.10	-0.23 ± 0.12	0.03 ± 0.06	0.07 ± 0.05	-0.02 ± 0.04	-0.01 ± 0.00	-0.02 ± 0.01	-0.01 ± 0.01	-0.03 ± 0.02	-0.04 ± 0.03	0.30 ± 0.15	3.02 ± 0.11
1312163	0.86 ± 0.28	0.10 ± 0.06	-0.01 ± 0.05	0.10 ± 0.03	0.04 ± 0.02	-0.05 ± 0.05	0.00 ± 0.01	-0.03 ± 0.01	-0.02 ± 0.01	-0.03 ± 0.02	-0.09 ± 0.04	1.77 ± 0.12	2.99 ± 0.13

=NOTE—All fluxes and uncertainties are given in units of μJy . Column 1: Source name. Column 2: K_s -band flux from the VIDEO survey. Column 3: H -band flux from the VIDEO survey. Column 4: J -band flux from the VIDEO survey. Column 5: Y -band flux from the VIDEO survey. Column 6: Z -band flux from the VIDEO survey. Column 7: u' -band flux from the wide tier of the CFHTLS survey (CFHTLS-W1). Column 8: g -band flux from the Ultradeep tier of DR1 of the HSC survey. Column 9: r -band flux from the Ultradeep tier of DR1 of the HSC survey. Column 10: i -band flux from the Ultradeep tier of DR1 of the HSC survey. Column 11: z -band flux from the Ultradeep tier of DR1 of the HSC survey. Column 12: y -band flux from the DeepDrill survey. Column 13: $3.6\mu\text{m}$ *Spitzer* IRAC flux from the DeepDrill survey. Column 14: $4.5\mu\text{m}$ *Spitzer* IRAC flux from the DeepDrill survey.

[†] The CFHTLS flux is based on the deeper CFHTLS-D1 tier and the HSC flux is based on the shallower Deep tier.

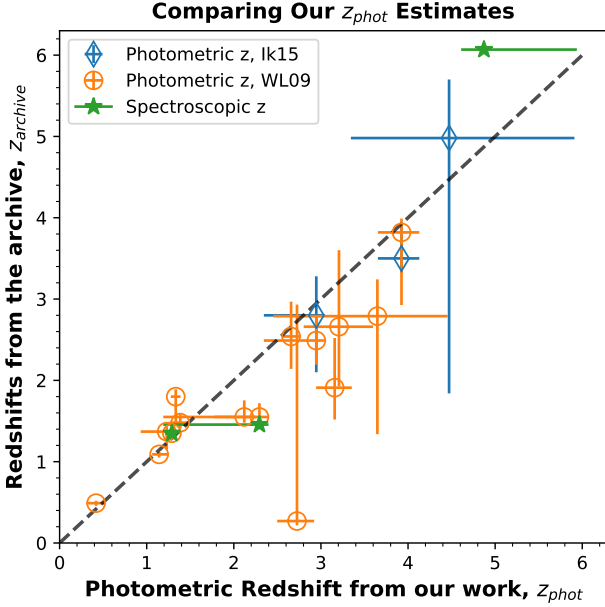


Figure 6. A comparison of the photometric redshifts evaluated in this work with redshift estimates from previous studies. A total of 18/26 sources have either photometric or spectroscopic redshifts available in the literature. The green points correspond to sources with spectroscopic redshifts. The orange and blue points have photometric redshift estimates published by Williams et al. (2009) and Ikarashi et al. (2015), respectively. The uncertainties from our work are smaller than in previous studies, highlighting our improved photometry through the use of the *Tractor* image modeling software.

tions in the photometry techniques used to obtain colors. La-
 porte et al. (2017) pointed out that the disagreement of the
 $K_s - [3.6]$ colors between their and Chen et al. (2016b)
 sample was mainly due to the differences in the *Spitzer* IRAC
 aperture correction methods. When the OIRTC color criteria
 were re-calibrated for their field galaxies, the new color-cuts
 were 80% complete. The *Tractor* forced photometry pre-
 sented in our work takes the point spread function of each
 band into account, thus removing the need for aperture cor-
 rections. Nevertheless, we still find a significant fraction of
 the sample occupying bluer $K_s - [3.6]$ colors, which may be
 due to the differences in the intrinsic properties of the faint
 and bright SMGs. Hence, additional checks are needed be-
 fore directly applying color cuts from the other studies. It
 would be useful to perform future studies which combine all
 the different faint SMGs and provide consistent photometry
 for all the comparison samples.

As mentioned above, the other reason could be the intrin-
 sic differences in the SEDs of bright and faint SMGs. The
 OIRTC color selection method is trained using bright SMGs,
 and the faint population in Chen et al. (2016a) does not have
 confirmed interferometric detections. Hence, the technique
 is targeting faint galaxies having SEDs similar to the bright

SMGs. To further support this, Hatsukade et al. (2015) found
 bluer colors for their sample of faint SMGs. Therefore, addi-
 tional study is needed, including spectroscopic follow-up, in
 order to better understand the colors of faint SMGs.

4.4. The UVJ color-color plot

At higher redshifts, where it is difficult to classify galaxies
 based on their morphologies, classifications via rest-frame
 broad-band colors have proven to be useful. Star-forming
 and quiescent galaxies show a bi-modality in rest-frame col-
 ors up to $z \sim 2.5$ in the UVJ color-color diagram (Labbé
 et al. 2005; Wuyts et al. 2007; Williams et al. 2009; Whitaker
 et al. 2011; Brammer et al. 2011; Patel et al. 2011). The qui-
 escent galaxies form a red clump called the “red sequence”,
 and star-forming galaxies fall on a diagonal line. The redder
 galaxies on the star-forming main sequence have higher dust
 extinction. The $U - V$ and $V - J$ colors of the DFSGs are
 both reddened by dust extinction. However, in the case of
 quiescent galaxies, only the $U - V$ colors are reddened due
 to the Balmer/4000 Å break, and the $V - J$ colors are bluer
 as compared to the $U - V$ (Chen et al. 2016b). Therefore,
 the $V - J$ color is a good proxy for dust extinction, and the
 two colors can separate DFSGs and red sequence quiescent
 galaxies up to $z \sim 2.5$.

Figure 8 shows the rest frame UVJ color diagram for our
 sample. The rest frame colors are estimated using EAZY as
 explained in Section 3.3. To estimate the uncertainties in the
 U , V , and J bands, we find the two nearest filters for each
 band, and add their errors in quadrature. Then, we calculate
 the uncertainties of the rest-frame colors using a simple error
 propagation rule. Here, we consider only measurement errors
 and exclude the errors in the SED templates and fitting.

The quiescent galaxy color cuts are taken from Williams
 et al. (2009). The color selection is defined as follows:

$$U - V > 1.3 \quad (1)$$

$$V - J < 1.6 \quad (2)$$

$$U - V > 0.88 \times (V - J) + 0.49 \quad (3)$$

The third criterion has a small dependence on redshift, and
 we used the equation for the redshift bin $1 < z < 2$. Five
 out of 26 galaxies are located within the quiescent box, and
 the rest of the sample has colors similar to the star-forming
 galaxies. When we compare the bi-color sequence from
 Williams et al. (2009), we see that our star-forming sample
 occupies redder $U - V$ and $V - J$ colors indicating the dusty
 and high-redshift nature of our sample.

4.5. Stacking of Undetected ALMA Sources

We used stacking to investigate the nature of the faint pop-
 ulation that was not individually detected in our photometric

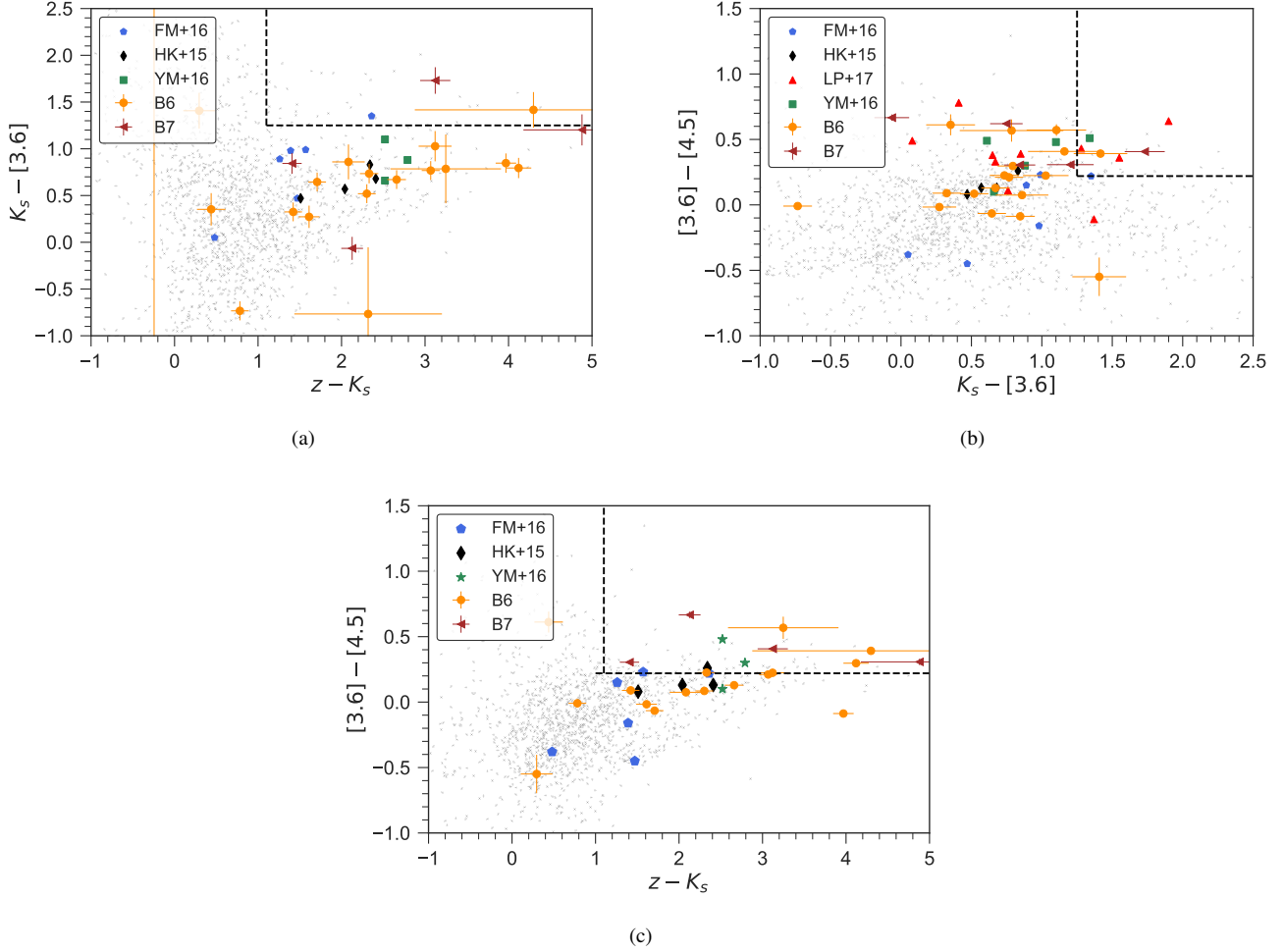


Figure 7. The plot shows the SMG OIRTC color selection criteria defined in [Chen et al. \(2016b\)](#). Each sub-figure is a color-color plot of the combination of z , K_s , $[3.6]$, and $[4.5]$ filters. Bright SMGs tend to occupy the reddest part of the color space due to the presence of dust. The black dotted line in each sub-figure is a color cut-off estimated by [Chen et al. \(2016b\)](#) using an ALMA sample of bright SMGs. The fraction of SMGs in the population redder than the color threshold is at least 5%. The yellow filled circles (B6), and brown horizontal triangles (B7) represent Band 6 and 7 sources in our sample, respectively. Other faint SMG samples are shown as follows:- YM+16 (Green squares) - [Yamaguchi et al. \(2016\)](#); HK+15 (Black diamonds) - [Hatsukade et al. \(2015\)](#); FM+16 (Blue pentagons) - [Fujimoto et al. \(2016\)](#); LP+17 (Red vertical triangles) - [Laporte et al. \(2017\)](#). The light gray symbols in the background show the field non-SMG galaxies found within all ALMA pointings. Our sample occupies a bluer color space than the OIRTC selection cut-off mainly due to the mail $K_s - [3.6] \mu m$ color. This shows that the optical-NIR color properties of our faint SMG population are different from the bright SMGs.

catalog. As the rate of contamination of the ALMA catalog by noise fluctuations is expected to be very small above 5σ , we stacked the DeepDrill IRAC data at the positions of the $> 5\sigma$ sources (60/176). We divided our sample into sources that were bright (> 1 mJy), or faint (< 1 mJy). We only detected $> 3\sigma$ emission in the IRAC $4.5 \mu m$ channel stack of the faint sources (Table 3) at the level of $0.34 \mu Jy$ ($AB = 25.3$). This indicates that the majority of the undetected population is extremely faint in the IRAC bands ($AB \gtrsim 25$), and is either of low stellar mass ($\lesssim 10^{10} M_\odot$ at $z = 2$) and/or highly reddened.

5. SUMMARY AND CONCLUSIONS

Table 3. Results of stacking $> 5\sigma$ ALMA objects that were undetected in the IRAC bands

Stack	Number	$3.6 \mu m$	$4.5 \mu m$
		AB mag	AB mag
All undetected	60	>26.1	>26.1
> 1 mJy	44	>25.8	>25.9
< 1 mJy	16	>25.5	25.3

In this paper, we have successfully demonstrated the use of archival ALMA observations to search for faint SMGs. The ALMA detections in the XMM-LSS field greater than 3.9σ

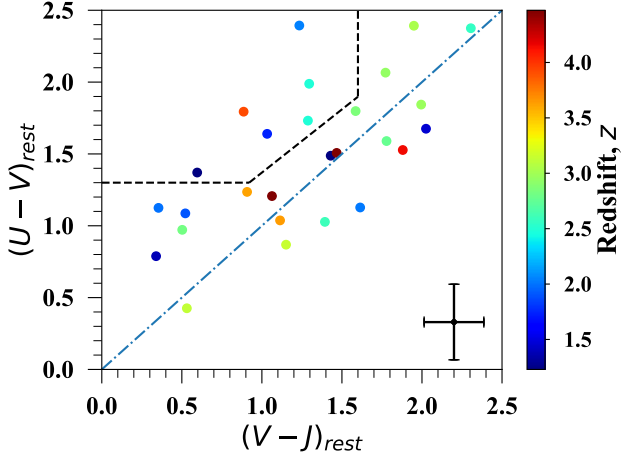


Figure 8. UVJ color selection diagram. The symbols are color coded based on their photometric redshifts and the color bar is shown on the right. Five out of the 26 galaxies lie in the quiescent galaxy clump. The blue dotted line is a proportionality line and is plotted to identify the diagonal track occupied by the star-forming galaxies. The black error-bar in the bottom-right corner shows the average uncertainties in the color estimation.

were cross-matched with the deep optical-NIR observations taken from SERVS/DeepDrill, VIDEO, CFHTLS, and HSC. We identify 26 sources with NIR counterparts, 15 of which are newly-identified faint SMGs. To further investigate the nature of this cosmologically important population, we have analyzed the basic properties of our sample. Of the total 26 sources, there are 16 faint SMGs ($S_{1.1\text{ mm}} < 1\text{ mJy}$) with a median flux of 0.57 mJy and 10 bright SMGs with a median flux of 2.44 mJy. Robust 13-band forced photometry using the *Tractor* image modeling code is available for our entire catalog.

The resulting photometric measurements were used to estimate photometric redshifts and rest-frame colors. Our sources have redshifts in the range of $0.4 < z_{\text{phot}} < 5.3$, with a median photometric redshifts of $\langle z \rangle = 2.72$ and 2.57 for Band 6 and 7, respectively. The median redshift and the average depth of our search are in good agreement with the predictions given in Béthermin et al. (2015).

We performed an optical-NIR triple-color selection that showed that most of our sample galaxies have bluer colors than the redder bright SMGs. Different color properties of faint SMGs could indicate different physical properties compared to their brighter counterparts. Based on the rest-frame UVJ colors, we found that most of the galaxies in our sample form the star-forming diagonal track on the UVJ diagram. Their colors are consistent with star-forming main sequence galaxies.

ALMA has made the discovery of this population of DS-FGs possible. We will continue mining publicly available

ALMA archival observations, and expand our search to the remaining five SERVS/DeepDrill fields to find a large sample of faint SMGs. We will include robust optical-NIR photometry along with far-IR *Herschel* observations to perform SED modeling of all the targets and estimate stellar masses, star formation rates, and other physical properties. Pilot studies (including this work) are unveiling the nature of the faint SMGs that dominate the CIB. Future large-scale surveys are essential to understanding the role of these galaxies in shaping galaxy evolution.

ACKNOWLEDGMENTS

The National Radio Astronomy Observatory is a facility of the National Science Foundation operated under cooperative agreement by Associated Universities, Inc. Support for this work was provided by the NSF through the Grote Reber Fellowship Program administered by Associated Universities, Inc./National Radio Astronomy Observatory. This paper makes use of the following ALMA data: ADS/JAO.ALMA #2011.0.00115.S, #2011.0.00648.S, #2011.0.00539.S, #2012.1.00326.S, #2012.1.00374.S, #2012.1.00934.S, #2013.1.00815.S, #2013.A.00021.S, #2015.1.01105.S. ALMA is a partnership of ESO (representing its member states), NSF (USA) and NINS (Japan), together with NRC (Canada) and NSC and ASIAA (Taiwan) and KASI (Republic of Korea), in cooperation with the Republic of Chile. The Joint ALMA Observatory is operated by ESO, AUI/NRAO and NAOJ. This work is based on observations made with the *Spitzer* Space Telescope, which is operated by the Jet Propulsion Laboratory, California Institute of Technology under a contract with NASA. K.N. acknowledges support provided by the grant associated with *Spitzer* proposal 11086. J.A. gratefully acknowledges support from the Science and Technology Foundation (FCT, Portugal) through the research grants PTDC/FIS-AST/2194/2012, PTDC/FIS-AST/29245/2017, UID/FIS/04434/2013 and UID/FIS/04434/2019.

The authors have made use of *ASTROPY*, a community-developed core PYTHON package for Astronomy [Astropy Collaboration et al. \(2013\)](#). We also used *MONTAGE*, which is funded by the National Science Foundation under Grant Number ACI-1440620, and was previously funded by the National Aeronautics and Space Administration’s Earth Science Technology Office, Computation Technologies Project, under Cooperative Agreement Number NCC5-626 between NASA and the California Institute of Technology. This research has made use of the NASA/IPAC Extragalactic Database (NED) which is operated by the Jet Propulsion Laboratory, California Institute of Technology, under contract with the National Aeronautics and Space Administration.

Facility: ALMA, *Spitzer*, CFHT, VISTA, Subaru

APPENDIX

A. THE ALMA ARCHIVAL PROJECTS

Nine ALMA projects satisfied our selection criteria given above and were publicly available. These projects were undertaken for entirely different science goals. The data is taken from [Ouchi et al. \(2013\)](#), who observed a giant starburst galaxy at redshift $z \sim 7$, called Himiko, at Band 6. The total integration time was about 3 hours reaching noise levels $\sim 19 \mu\text{Jy beam}^{-1}$. Other deep maps were taken from ALMA 2013.1.00815.S ([Willott et al. 2015](#)). They have investigated continuum dust emission and [CII] line detections for three more UV-luminous galaxies similar to Himiko found at $z \sim 6$. The total time on the source is about an hour and a half with rms noise levels of $18 \mu\text{Jy beam}^{-1}$. The ALMA 2012.1.00934.S [PI: Phillip Best] covers four maps in the XMM-field to study the star formation activity in moderately star-forming galaxies at $z \sim 2.53$ using CO molecular line emission. [Ikarashi et al. \(2015\)](#) have observed 30 potential high- z SMG candidates selected from the AzTEC survey. These galaxies are highly likely to be at $z > 3$. This project, ALMA 2012.1.00326.S, has 4 minutes on source time with rms levels between 135-65 $\mu\text{Jy beam}^{-1}$. A 100-minute observation was undertaken by [Inoue et al. \(2016\)](#) [ALMA 2012.1.00374.S, PI: Kazuaki Ota] to study the state of the epoch of reionization and star formation activity at $z \sim 7$ using spectroscopically confirmed galaxies at that redshift. The same target was observed for another 75 minutes in the project ALMA 2013.A.00021.S to improve the sensitivity of [CII] line detection. The data from ALMA 2011.0.00648.S is taken to study interstellar medium of 20 star-forming galaxies at $z \sim 1.4$ ([Seko et al. 2016a,b](#)). The typical rms noise levels range from 60-100 $\mu\text{Jy beam}^{-1}$ with 10 minutes of the on-source time. [Pentericci et al. \(2016\)](#) studied a very high redshift galaxy ($z \sim 7$) to understand the role of high- z galaxies in the epoch of reionization. The target was observed for 35 minutes which resulted in 20 μJy noise level. The project 2011.0.00539.S was used to study the ALMA properties of the lensed, bright submillimeter galaxies selected from *Herschel*. The time on each map is about a minute, with typical rms noise levels of 250 $\mu\text{Jy beam}^{-1}$. This ALMA project is the only Band 7 observations we have used in our search.

B. PHOTOMETRY CONSISTENCY CHECK

As we compare colors of the faint SMGs with the selection criteria specified by [Chen et al. \(2016b\)](#), it is essential to perform a consistency check within both the data catalogs. Our *Tractor* method utilizes VIDEO catalog whose photometry is in the AB magnitude system. The sample of [Chen et al. \(2016b\)](#) is taken from UKIDSS-Ultra Deep Survey (UDS) data release 8 (DR8). We compare J , H , and K bands from the publicly available DR8¹⁰ with the VIDEO catalog in Figure 10. The data points plotted here are the field galaxies lying within the ALMA pointings used in our search. The positions of those objects were cross-matched with the publicly available UDS DR8 catalog. We show Petrosian magnitudes for both the catalogs in the AB system. Overall, there is a good level of agreement between our photometry and the UDS photometry. We can see a small offset between the K filter used in the UKIDSS-UDS surveys and the K_s filter used in the VIDEO survey. The offset is mainly due to the differences in the filter response functions of K and K_s .

C. LIST OF CONTINUUM MAPS FROM THE ALMA ARCHIVE

Table 4 provides a list of continuum maps used in the search of the faint SMG population. There are 75 individual pointings used in our work, and the sky position, date of observation, project ID, central frequency of observation, clean beam size, and rms noise levels are given in the paper.

¹⁰ We used the following link to access the UDS photometry. http://wsa.roe.ac.uk:8080/wsa/crossID_form.jsp

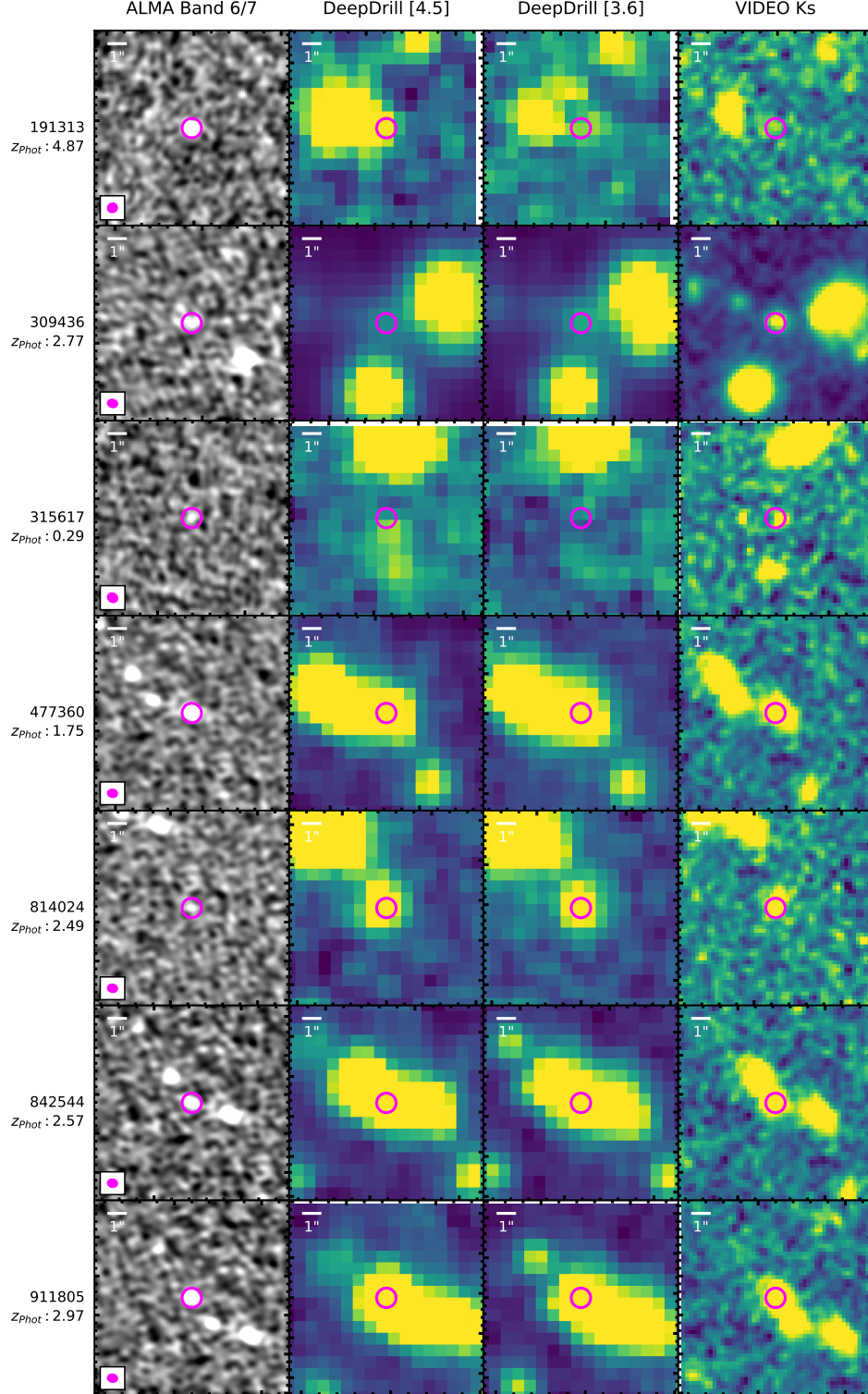
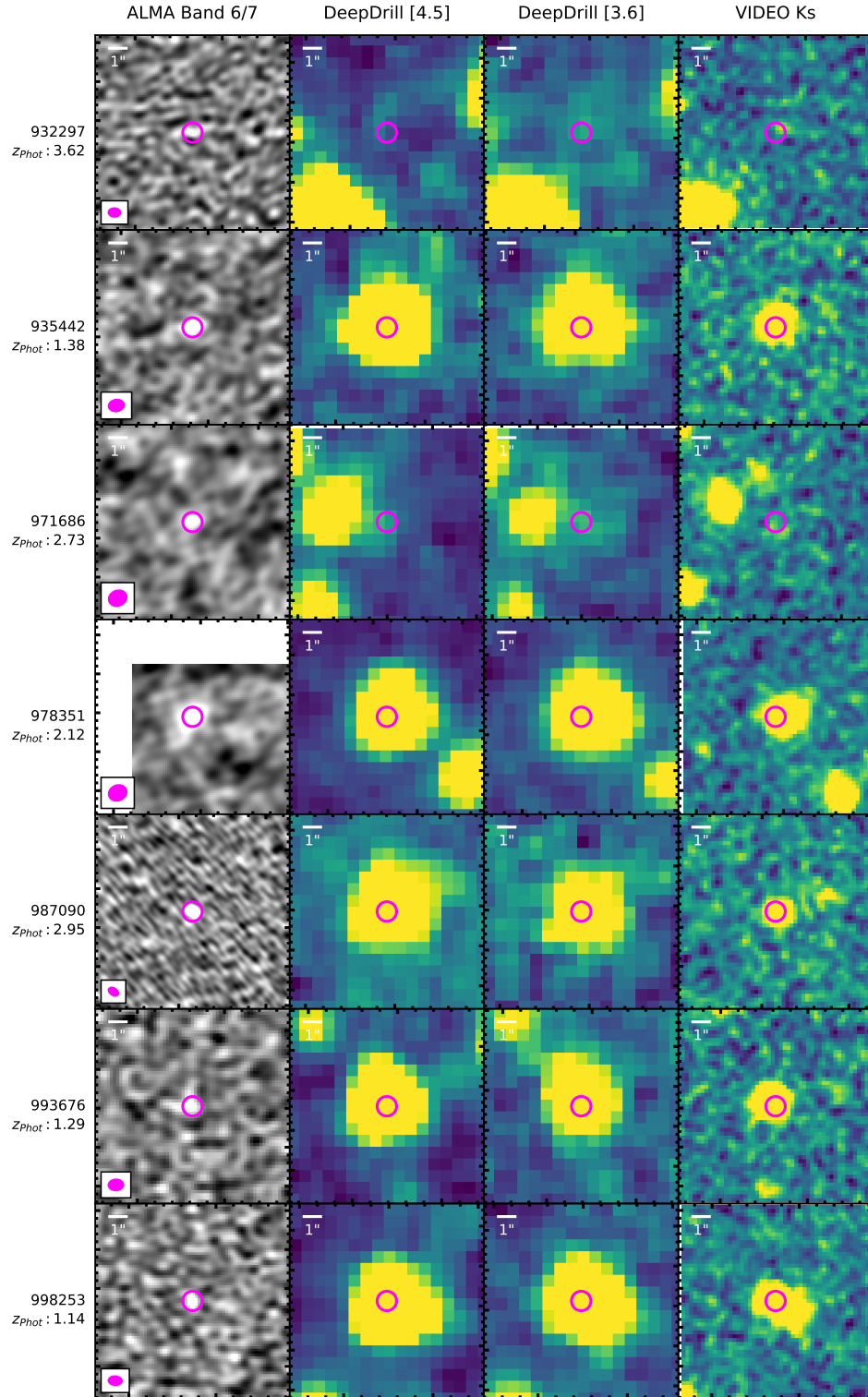
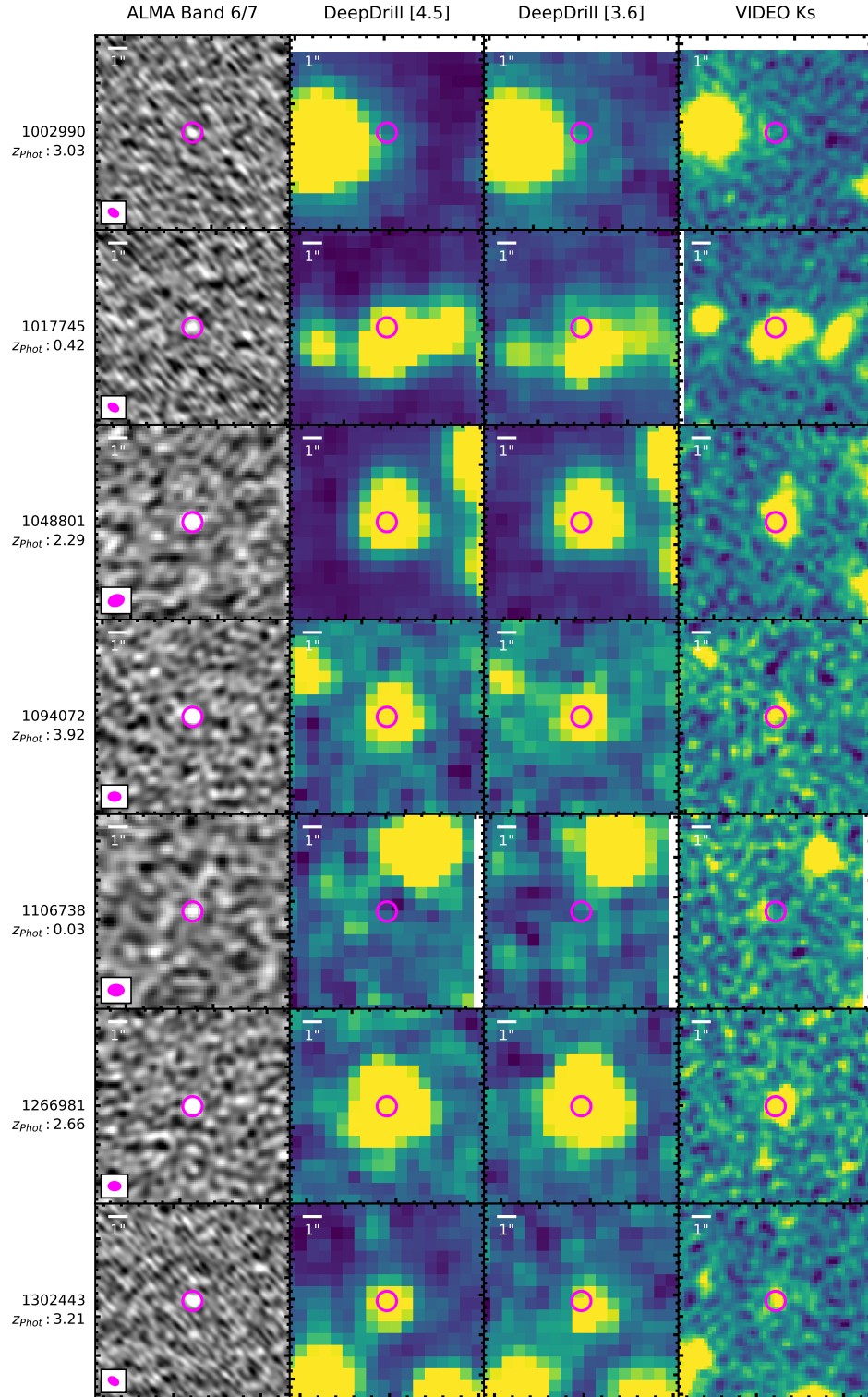


Figure 9. Image snapshots of our entire sample in four bands. The grayscale image on the left is the ALMA Band 6/7 image obtained from the archive. The rest are the *Spitzer* 4.5 μm , *Spitzer* 3.6 μm , and VIDEO K_s image left to right. The magenta circle in each image indicates the position of the ALMA source. Our photometric redshift estimates are also given on the left. Each cutout has a size of $10'' \times 10''$

Figure 9. *Continued*

Figure 9. *Continued*

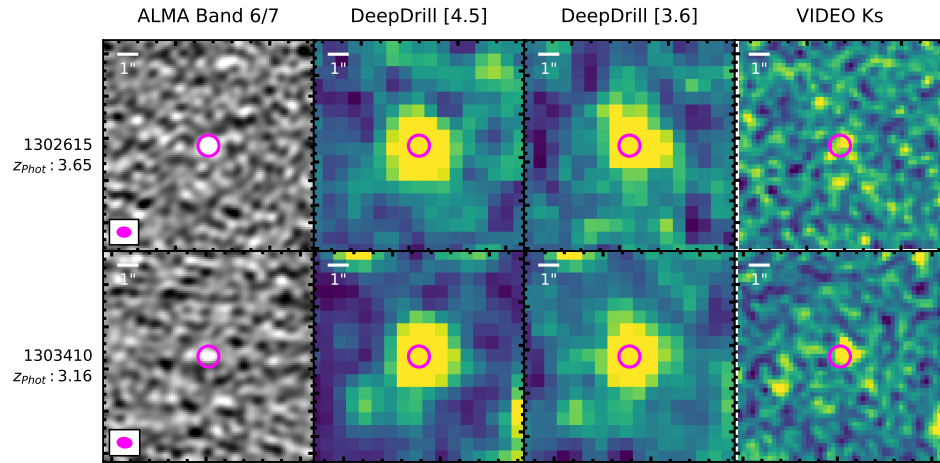


Figure 9. *Continued*

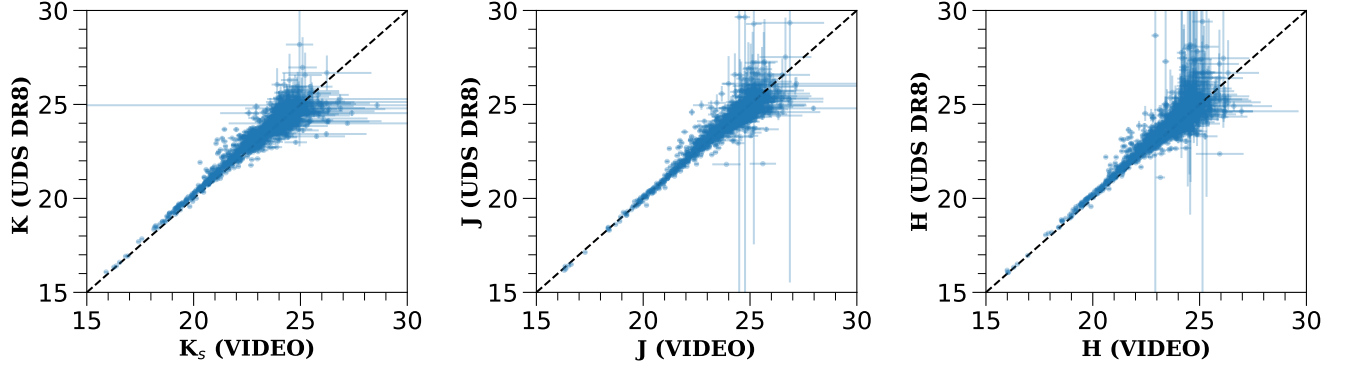


Figure 10. The plot shows a comparison of the photometry from our work and the publicly available UKIDSS-UDS DR8 catalog. Our photometry is derived from the VIDEO catalog (See Section 3.2). We show Petrosian magnitudes in the AB system for both catalogs. The black dashed line is the equality line. We see overall good agreement between both the observations. A slight offset in the K band is mainly due to the differences in the filter response function.

Table 4. Details of the archival observations and individual pointings

Index	Map	RA (J2000)	Dec (J2000)	Date of Observation (yyyy – mm – dd)	Project ID	ν_{obs} (GHz)	λ_{obs} (mm)	Resolving Beam ($'' \times ''$)	RMS Noise ($\mu Jy \text{ beam}^{-1}$)
0	CLM1	02h28m02.970s	-04d16m18.30s	2014-06-16	2013.1.00815.S	258	1.16	0.53×0.46	15.42
1	HiZELS-UDS-NBK-1147	02h17m37.000s	-05d09m12.00s	2014-01-27	2012.1.00934.S	222	1.35	1.64×0.7	58.27
2	HiZELS-UDS-NBK-1196	02h17m40.120s	-05d12m02.35s	2014-01-27	2012.1.00934.S	222	1.35	1.65×0.7	60.39
3	HiZELS-UDS-NBK-1348	02h17m51.470s	-05d10m36.40s	2014-01-27	2012.1.00934.S	222	1.35	1.65×0.7	59.21
4	HiZELS-UDS-NBK-8806	02h17m18.650s	-05d07m54.20s	2014-01-27	2012.1.00934.S	222	1.35	1.64×0.7	59.53
5	Himiko	02h17m57.563s	-05d08m44.45s	2012-07-15	2011.0.00115.S	259	1.16	0.71×0.48	19.86
6	SXDF1100.013	02h16m46.210s	-05d03m47.83s	2013-11-19	2012.1.00326.S	265	1.13	0.57×0.38	81.4
7	SXDF1100.019	02h17m15.920s	-05d04m03.13s	2013-11-19	2012.1.00326.S	265	1.13	0.57×0.38	81.23
8	SXDF1100.027	02h17m20.550s	-05d08m42.36s	2013-11-19	2012.1.00326.S	265	1.13	0.57×0.38	80.98
9	SXDF1100.036	02h18m00.700s	-05d07m29.69s	2013-11-19	2012.1.00326.S	265	1.13	0.57×0.38	81.5
10	SXDF1100.039	02h18m30.590s	-05d01m16.09s	2013-11-19	2012.1.00326.S	265	1.13	0.57×0.38	79.86
11	SXDF1100.045	02h18m15.350s	-04d54m03.36s	2013-11-19	2012.1.00326.S	265	1.13	0.57×0.38	79.46
12	SXDF1100.049	02h17m33.310s	-04d57m02.02s	2013-11-19	2012.1.00326.S	265	1.13	0.57×0.38	81.66
13	SXDF1100.053	02h16m48.170s	-04d58m56.66s	2013-11-19	2012.1.00326.S	265	1.13	0.57×0.38	82.26
14	SXDF1100.060	02h17m37.700s	-05d08m23.17s	2013-11-30	2012.1.00326.S	265	1.13	0.68×0.48	137.39
15	SXDF1100.063	02h17m35.990s	-04d52m18.15s	2013-11-19	2012.1.00326.S	265	1.13	0.57×0.38	80.8
16	SXDF1100.073	02h18m10.270s	-05d11m26.18s	2013-11-30	2012.1.00326.S	265	1.13	0.68×0.48	141.14
17	SXDF1100.082	02h17m58.290s	-04d59m11.16s	2013-11-30	2012.1.00326.S	265	1.13	0.69×0.48	141.18
18	SXDF1100.083	02h17m11.830s	-05d03m59.71s	2013-11-30	2012.1.00326.S	265	1.13	0.69×0.48	143.26
19	SXDF1100.090	02h17m23.660s	-04d57m24.06s	2013-11-30	2012.1.00326.S	265	1.13	0.69×0.48	139.67
20	SXDF1100.101	02h18m35.580s	-05d10m02.67s	2013-11-30	2012.1.00326.S	265	1.13	0.69×0.48	139.46
21	SXDF1100.104	02h18m04.930s	-05d08m19.32s	2013-11-30	2012.1.00326.S	265	1.13	0.68×0.48	141.65
22	SXDF1100.109	02h17m44.200s	-05d08m05.49s	2013-11-30	2012.1.00326.S	265	1.13	0.69×0.48	140.09
23	SXDF1100.110	02h18m11.930s	-05d14m20.94s	2013-11-30	2012.1.00326.S	265	1.13	0.69×0.48	141.69
24	SXDF1100.123	02h17m33.080s	-04d48m51.89s	2013-11-30	2012.1.00326.S	265	1.13	0.69×0.48	138.85
25	SXDF1100.127	02h18m14.490s	-04d56m12.80s	2013-11-30	2012.1.00326.S	265	1.13	0.64×0.46	65.92
26	SXDF1100.154	02h18m16.350s	-05d15m28.80s	2013-11-30	2012.1.00326.S	265	1.13	0.64×0.46	63.9
27	SXDF1100.174	02h18m43.870s	-04d57m33.62s	2013-11-30	2012.1.00326.S	265	1.13	0.64×0.46	64.95
28	SXDF1100.179	02h17m58.610s	-04d45m49.13s	2013-11-30	2012.1.00326.S	265	1.13	0.64×0.46	64.43
29	SXDF1100.230	02h17m59.910s	-04d46m50.05s	2013-11-30	2012.1.00326.S	265	1.13	0.64×0.46	64.6
30	SXDF1100.231	02h18m53.030s	-04d58m14.74s	2013-11-19	2012.1.00326.S	265	1.13	0.64×0.46	65.54
31	SXDF1100.233	02h17m52.690s	-05d20m31.72s	2013-11-30	2012.1.00326.S	265	1.13	0.57×0.38	81.82
32	SXDF1100.250	02h18m26.970s	-05d14m38.61s	2013-11-30	2012.1.00326.S	265	1.13	0.64×0.46	64.78
33	SXDF1100.253				2012.1.00326.S	265	1.13	0.64×0.46	64.45

Table 4 continued

Table 4 (continued)

Index	Map	RA (J2000)	Dec (J2000)	Date of Observation (yyyy-mm-dd)	Project ID	ν_{obs} (GHz)	λ_{obs} (mm)	Resolving Beam ($'' \times ''$)	RMS Noise ($\mu Jy beam^{-1}$)
34	SXDF1100.276	02h18m33.930s	-04d54m23.85s	2013-11-30	2012.1.00326.S	265	1.13	0.64×0.46	66.35
35	SXDF1100.277	02h17m24.090s	-05d20m21.94s	2013-11-30	2012.1.00326.S	265	1.13	0.64×0.46	63.16
36	SXDF220GHZ	02h18m56.536s	-05d19m58.92s	2014-05-03	2012.1.00374.S	224	1.33	0.82×0.62	12.56
37	SXDF-NB1	02h18m56.536s	-05d19m58.92s	2015-12-27	2013.A.00021.S	224	1.33	1.94×1.07	15.1
38	SXDS1_13015	02h17m13.617s	-05d09m39.82s	2012-08-15	2011.0.00648.S	243	1.23	0.8×0.58	100.87
39	SXDS1_1723	02h17m32.701s	-05d13m16.47s	2012-08-26	2011.0.00648.S	240	1.25	1.11×0.59	111.28
40	SXDS1_33244	02h16m47.397s	-05d03m28.09s	2012-08-26	2011.0.00648.S	240	1.25	0.95×0.59	77.72
41	SXDS1_35572	02h17m34.652s	-05d02m38.97s	2012-08-11	2011.0.00648.S	236	1.27	0.78×0.58	46.17
42	SXDS1_59863	02h17m45.877s	-04d54m37.60s	2012-08-15	2011.0.00648.S	243	1.23	0.81×0.58	95.02
43	SXDS1_59914	02h17m12.977s	-04d54m40.40s	2012-08-26	2011.0.00648.S	240	1.25	1.04×0.59	109.0
44	SXDS1_67002	02h19m02.654s	-04d49m55.83s	2012-08-15	2011.0.00648.S	243	1.23	0.83×0.57	97.8
45	SXDS1_68849	02h17m00.276s	-04d48m14.53s	2012-08-26	2011.0.00648.S	240	1.25	0.85×0.6	96.21
46	SXDS1_79518	02h18m59.059s	-04d51m24.91s	2012-08-26	2011.0.00648.S	240	1.25	0.9×0.6	99.08
47	SXDS1	02h17m05.789s	-04d51m25.68s	2012-08-09	2011.0.00648.S	231	1.3	0.8×0.67	64.28
48	SXDS2_13316	02h17m39.035s	-04d44m41.75s	2012-08-15	2011.0.00648.S	243	1.23	0.81×0.57	92.28
49	SXDS2_22198	02h17m53.416s	-04d42m53.42s	2012-08-11	2011.0.00648.S	236	1.27	0.81×0.58	44.84
50	SXDS2	02h17m24.356s	-05d00m44.85s	2012-08-09	2011.0.00648.S	231	1.3	0.8×0.66	63.38
51	SXDS3_101746	02h18m04.178s	-05d19m38.28s	2012-08-26	2011.0.00648.S	240	1.25	0.93×0.6	99.25
52	SXDS3_103139	02h16m57.652s	-05d14m34.86s	2012-08-11	2011.0.00648.S	236	1.27	0.77×0.58	46.08
53	SXDS3_110465	02h18m20.953s	-05d19m07.71s	2012-08-26	2011.0.00648.S	240	1.25	0.99×0.6	99.74
54	SXDS3	02h17m13.683s	-05d04m07.66s	2012-08-09	2011.0.00648.S	231	1.3	0.81×0.66	60.34
55	SXDS5_19723	02h16m24.372s	-05d09m18.05s	2012-08-11	2011.0.00648.S	236	1.27	0.77×0.58	45.41
56	SXDS5_28019	02h16m08.532s	-05d06m15.61s	2012-08-11	2011.0.00648.S	236	1.27	0.78×0.58	46.36
57	SXDS5_9364	02h16m33.807s	-05d13m44.68s	2012-08-15	2011.0.00648.S	243	1.23	0.81×0.57	97.7
58	UDS16	02h17m25.474s	-05d11m08.25s	2016-03-31	2015.1.01105.S	241	1.24	0.96×0.8	21.5
59	WMH5	02h26m27.030s	-04d52m38.30s	2014-06-16	2013.1.00815.S	262	1.14	0.5×0.48	18.05
60	XMMF10	02h16m31.850s	-05d53m22.20s	2012-06-17	2011.0.00539.S	343	0.87	0.51×0.41	220.03
61	XMMF11	02h21m35.220s	-06d26m16.97s	2012-06-17	2011.0.00539.S	343	0.87	0.51×0.41	261.51
62	XMMF12	02h22m50.830s	-03d24m13.81s	2012-06-17	2011.0.00539.S	342	0.87	0.49×0.41	212.05
63	XMMF13	02h18m41.550s	-03d50m01.90s	2012-06-17	2011.0.00539.S	343	0.87	0.51×0.41	227.81
64	XMMF14	02h20m29.140s	-06d48m45.89s	2012-06-17	2011.0.00539.S	343	0.87	0.51×0.41	236.57
65	XMMF15	02h22m05.540s	-07d07m27.20s	2012-06-17	2011.0.00539.S	343	0.87	0.51×0.41	212.96
66	XMMF16	02h19m42.910s	-05d24m32.54s	2012-06-17	2011.0.00539.S	343	0.87	0.51×0.41	224.83
67	XMMF17	02h19m18.400s	-03d10m51.30s	2012-06-17	2011.0.00539.S	343	0.87	0.51×0.42	259.53
68	XMMF18	02h29m44.790s	-03d41m10.17s	2012-06-17	2011.0.00539.S	343	0.87	0.52×0.41	300.12
69	XMMF19	02h20m21.610s	-01d53m29.12s	2012-06-17	2011.0.00539.S	343	0.87	0.52×0.42	277.51

Table 4 continued

Table 4 (*continued*)

Index	Map	RA (J2000)	Dec (J2000)	Date of Observation (<i>yyyy-mm-dd</i>)	Project ID	ν_{obs} (GHz)	λ_{obs} (mm)	Resolving Beam ($'' \times ''$)	RMS Noise ($\mu\text{Jy beam}^{-1}$)
70	XMMF4	02h20m16.689s	-06d01m44.38s	2012-06-17	2011.0.00539.S	343	0.87	0.51×0.41	262.64
71	XMMF5	02h22m01.576s	-03d33m40.60s	2012-06-17	2011.0.00539.S	343	0.87	0.52×0.41	233.23
72	XMMF6	02h25m48.210s	-04d17m51.10s	2012-06-17	2011.0.00539.S	343	0.87	0.51×0.41	254.89
73	XMMF7	02h18m53.100s	-06d33m23.70s	2012-06-17	2011.0.00539.S	343	0.87	0.51×0.41	219.54
74	XMMF8	02h30m05.980s	-03d41m52.70s	2012-06-17	2011.0.00539.S	343	0.87	0.52×0.41	254.45

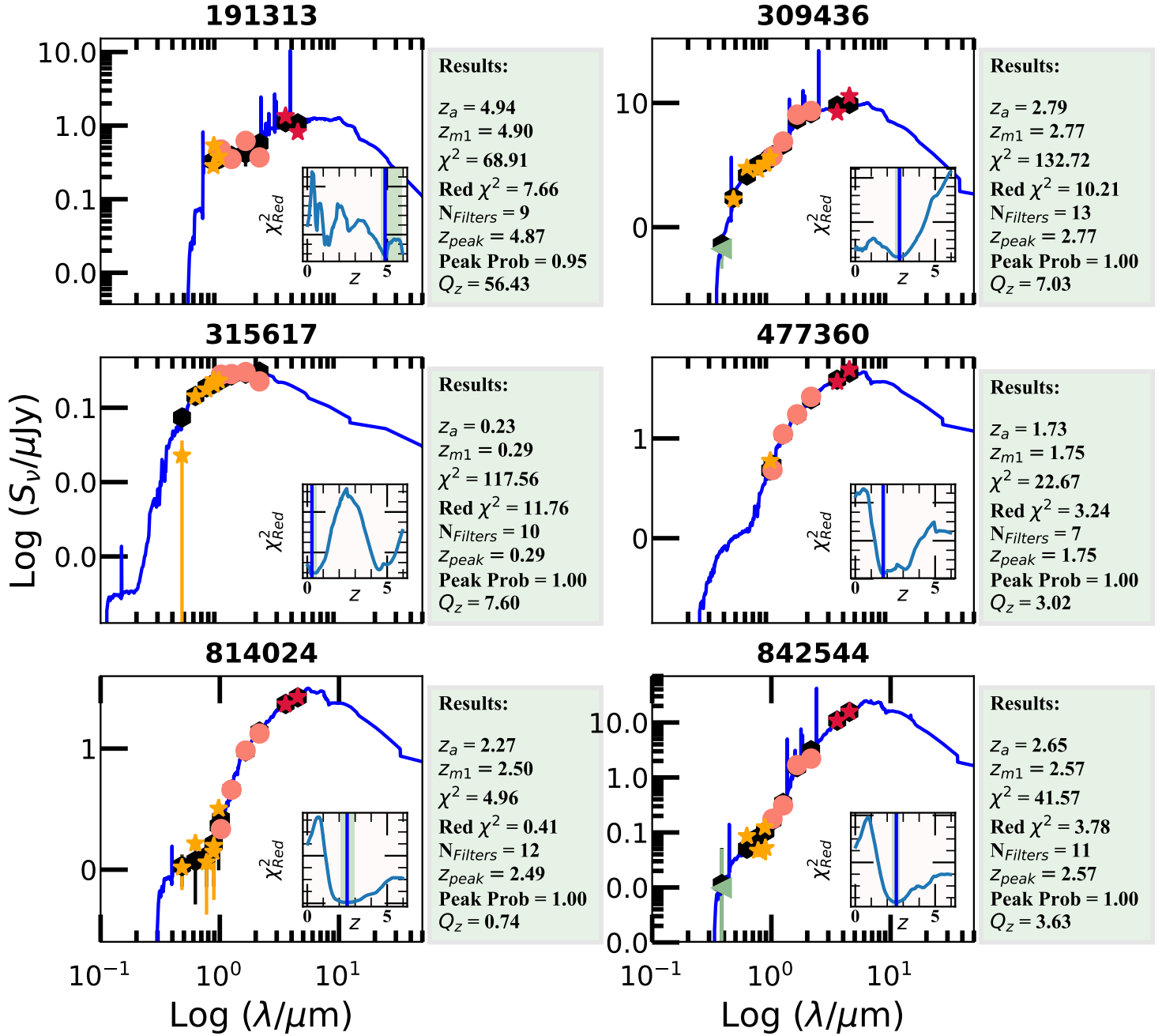


Figure 11. The figure sets show photometric redshift fitting of the entire sample. Different colored symbols correspond to the observed 13-band photometry, which is obtained using the *Tractor* image modeling code (Section 3.2). Red stars highlight *Spitzer* DeepDrill measurements at 3.6 and 4.5 μm , orange circles denote measurements from the VIDEO survey, the green triangle represents the optical *u*-band data from CFHTLS, and the yellow stars mark the optical data points from HSC. The blue solid line is the actual SED fit, and the black filled circles show the estimated template flux for each filter. The green box on the right lists key output parameters from EAZY. The inset figure shows the χ^2 distribution of the fit at each redshift bin. The blue vertical line shows the peak of the redshift distribution after applying the prior, and the light green regions are the 95% confidence intervals of the fit.

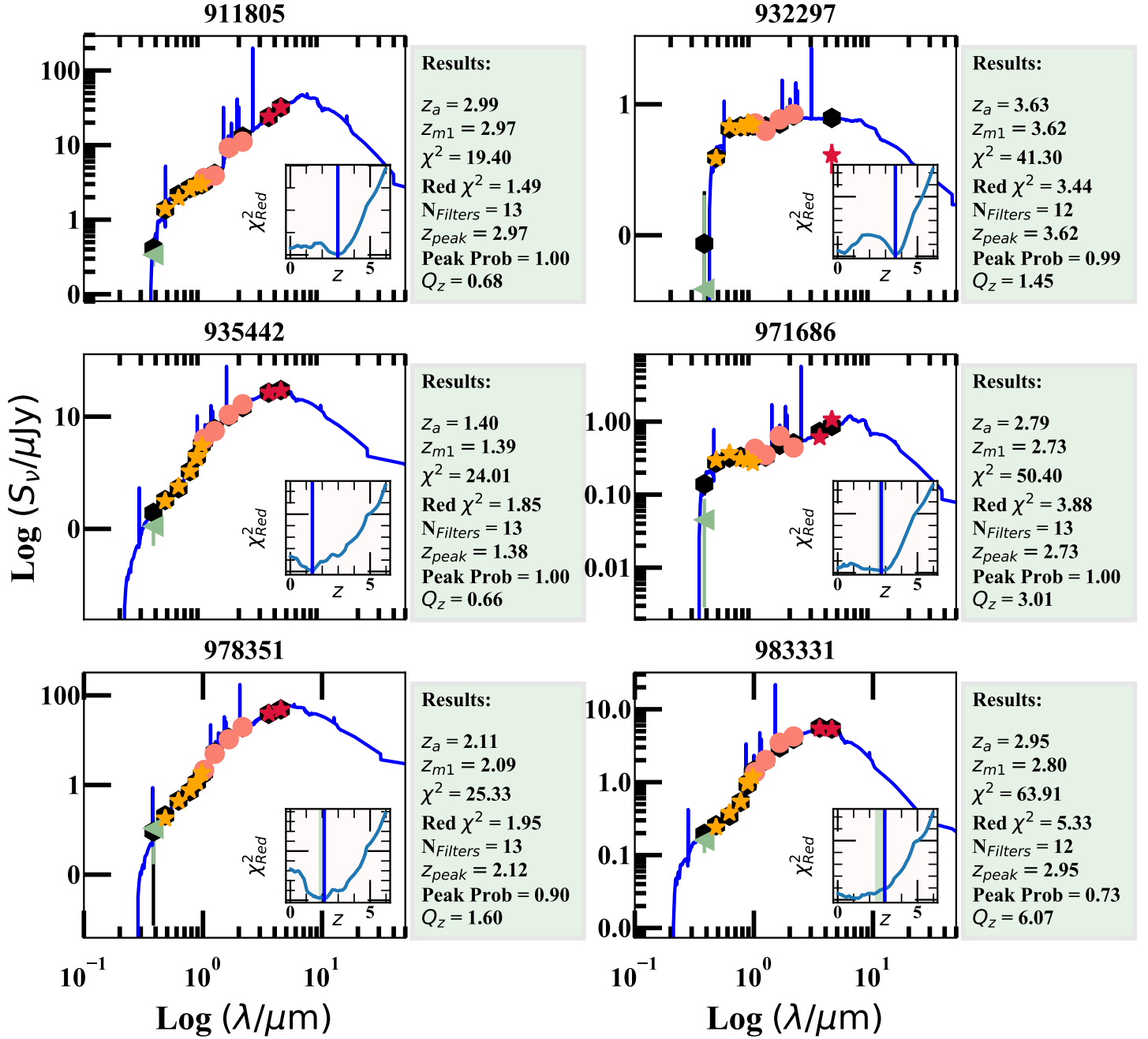


Figure 11. Continued

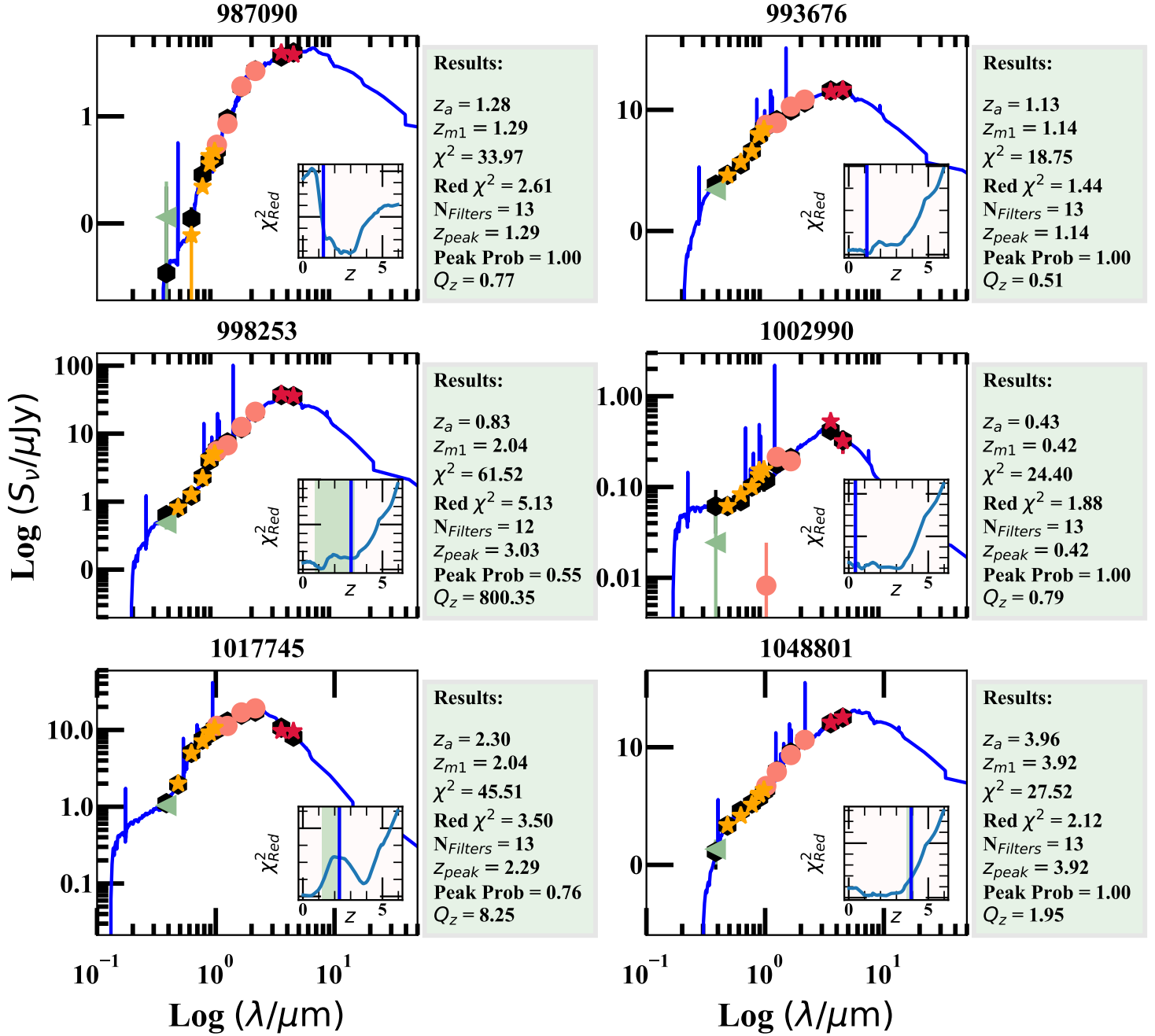


Figure 11. Continued

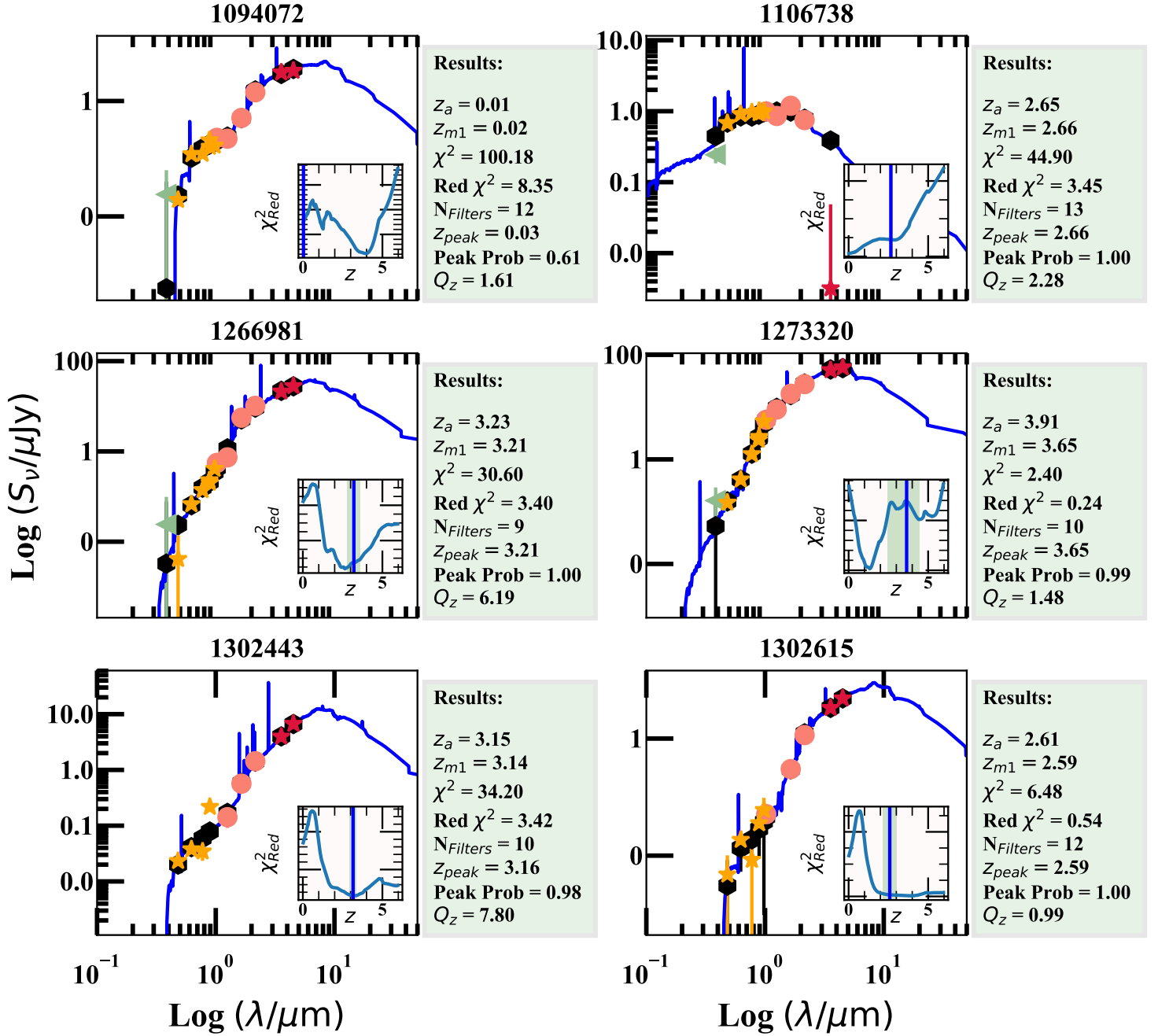


Figure 11. Continued

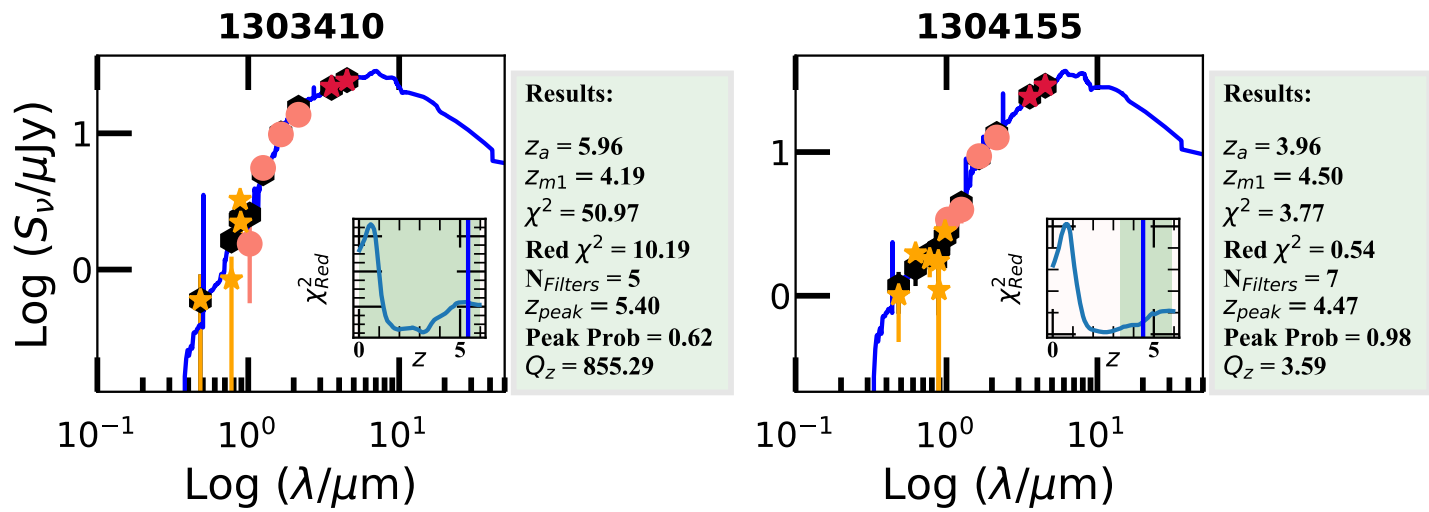


Figure 11. Continued

REFERENCES

- Aihara, H., Armstrong, R., Bickerton, S., et al. 2017, ArXiv e-prints, arXiv:1702.08449
- Alaghband-Zadeh, S., Chapman, S. C., Swinbank, A. M., et al. 2012, *MNRAS*, 424, 2232
- Alberts, S., Wilson, G. W., Lu, Y., et al. 2013, *MNRAS*, 431, 194
- Aravena, M., Decarli, R., Walter, F., et al. 2016, *ApJ*, 833, 68
- Aretxaga, I., Wilson, G. W., Aguilar, E., et al. 2011, *MNRAS*, 415, 3831
- Astropy Collaboration, Robitaille, T. P., Tollerud, E. J., et al. 2013, *A&A*, 558, A33
- Austermann, J. E., Dunlop, J. S., Perera, T. A., et al. 2010, *MNRAS*, 401, 160
- Banerji, M., Chapman, S. C., Smail, I., et al. 2011, *MNRAS*, 418, 1071
- Barger, A. J., Cowie, L. L., Sanders, D. B., et al. 1998, *Nature*, 394, 248
- Barger, A. J., Wang, W.-H., Cowie, L. L., et al. 2012, *ApJ*, 761, 89
- Bertoldi, F., Carilli, C., Aravena, M., et al. 2007, *ApJS*, 172, 132
- Béthermin, M., De Breuck, C., Sargent, M., & Daddi, E. 2015, *A&A*, 576, L9
- Biggs, A. D., Ivison, R. J., Ibar, E., et al. 2011, *MNRAS*, 413, 2314
- Blain, A. W., Jameson, A., Smail, I., et al. 1999, *MNRAS*, 309, 715
- Blain, A. W., Smail, I., Ivison, R. J., Kneib, J.-P., & Frayer, D. T. 2002, *PhR*, 369, 111
- Brammer, G. B., van Dokkum, P. G., & Coppi, P. 2008, *ApJ*, 686, 1503
- Brammer, G. B., Whitaker, K. E., van Dokkum, P. G., et al. 2011, *ApJ*, 739, 24
- Brisbin, D., Miettinen, O., Aravena, M., et al. 2017, *A&A*, 608, A15
- Bussmann, R. S., Riechers, D., Fialkov, A., et al. 2015, *ApJ*, 812, 43
- Carniani, S., Maiolino, R., De Zotti, G., et al. 2015, *A&A*, 584, A78
- Casey, C. M., Narayanan, D., & Cooray, A. 2014, *PhR*, 541, 45
- Casey, C. M., Chen, C.-C., Cowie, L. L., et al. 2013, *MNRAS*, 436, 1919
- Chapin, E. L., Chapman, S. C., Coppin, K. E., et al. 2011, *MNRAS*, 411, 505
- Chapman, S. C., Blain, A. W., Smail, I., & Ivison, R. J. 2005, *ApJ*, 622, 772
- Chapman, S. C., Scott, D., Borys, C., & Fahlman, G. G. 2002, *MNRAS*, 330, 92
- Chapman, S. C., Smail, I., Blain, A. W., & Ivison, R. J. 2004, *ApJ*, 614, 671
- Chen, C.-C., Cowie, L. L., Barger, A. J., et al. 2013a, *ApJ*, 776, 131
- . 2013b, *ApJ*, 762, 81
- Chen, C.-C., Cowie, L. L., Barger, A. J., Wang, W.-H., & Williams, J. P. 2014, *ApJ*, 789, 12
- Chen, C.-C., Smail, I., Swinbank, A. M., et al. 2015, *ApJ*, 799, 194
- . 2016a, *ApJ*, 831, 91
- Chen, C.-C., Smail, I., Ivison, R. J., et al. 2016b, *ApJ*, 820, 82
- Coppin, K., Chapin, E. L., Mortier, A. M. J., et al. 2006, *MNRAS*, 372, 1621
- Cowie, L. L., Barger, A. J., & Kneib, J.-P. 2002, *AJ*, 123, 2197
- Cowie, L. L., González-López, J., Barger, A. J., et al. 2018, *ApJ*, 865, 106
- Daddi, E., Cimatti, A., Renzini, A., et al. 2004, *ApJ*, 617, 746
- Dole, H., Lagache, G., Puget, J.-L., et al. 2006, *A&A*, 451, 417
- Dunlop, J. S., McLure, R. J., Yamada, T., et al. 2004, *MNRAS*, 350, 769
- Dunlop, J. S., McLure, R. J., Biggs, A. D., et al. 2017, *MNRAS*, 466, 861
- Engel, H., Tacconi, L. J., Davies, R. I., et al. 2010, *ApJ*, 724, 233
- Ezawa, H., Kawabe, R., Kohno, K., & Yamamoto, S. 2004, in *Proc. SPIE*, Vol. 5489, Ground-based Telescopes, ed. J. M. Oschmann, Jr., 763–772
- Franceschini, A., Toffolatti, L., Mazzei, P., Danese, L., & de Zotti, G. 1991, *A&AS*, 89, 285
- Franco, M., Elbaz, D., Béthermin, M., et al. 2018, ArXiv e-prints, arXiv:1803.00157
- Fu, H., Cooray, A., Feruglio, C., et al. 2013, *Nature*, 498, 338
- Fujimoto, S., Ouchi, M., Ono, Y., et al. 2016, *ApJS*, 222, 1
- Furusawa, H., Kosugi, G., Akiyama, M., et al. 2008, *ApJS*, 176, 1
- Geach, J. E., Chapin, E. L., Coppin, K. E. K., et al. 2013, *MNRAS*, 432, 53
- Geach, J. E., Dunlop, J. S., Halpern, M., et al. 2017, *MNRAS*, 465, 1789
- González-López, J., Bauer, F. E., Romero-Cañizales, C., et al. 2017, *A&A*, 597, A41
- Greve, T. R., Ivison, R. J., Bertoldi, F., et al. 2004, *MNRAS*, 354, 779
- Gwyn, S. D. J. 2012, *AJ*, 143, 38
- Hatsukade, B., Ohta, K., Seko, A., Yabe, K., & Akiyama, M. 2013, *ApJL*, 769, L27
- Hatsukade, B., Ohta, K., Yabe, K., et al. 2015, *ApJ*, 810, 91
- Hatsukade, B., Kohno, K., Aretxaga, I., et al. 2011, *MNRAS*, 411, 102
- Hauser, M. G., Arendt, R. G., Kelsall, T., et al. 1998, *ApJ*, 508, 25
- Hopkins, A. M., Whiting, M. T., Seymour, N., et al. 2015, *PASA*, 32, e037
- Hsu, L.-Y., Cowie, L. L., Chen, C.-C., Barger, A. J., & Wang, W.-H. 2016, *ApJ*, 829, 25
- Hughes, D. H., Serjeant, S., Dunlop, J., et al. 1998, *Nature*, 394, 241
- Ikarashi, S., Ivison, R. J., Caputi, K. I., et al. 2015, *ApJ*, 810, 133
- Inoue, A. K., Tamura, Y., Matsuo, H., et al. 2016, *Science*, 352, 1559

- Iverson, R. J., Smail, I., Le Borgne, J.-F., et al. 1998, *MNRAS*, 298, 583
- Iverson, R. J., Greve, T. R., Smail, I., et al. 2002, *MNRAS*, 337, 1
- Iverson, R. J., Greve, T. R., Dunlop, J. S., et al. 2007, *MNRAS*, 380, 199
- Iverson, R. J., Smail, I., Amblard, A., et al. 2012, *MNRAS*, 425, 1320
- Jarvis, M. J., Bonfield, D. G., Bruce, V. A., et al. 2013, *MNRAS*, 428, 1281
- Johansson, D., Sigurdarson, H., & Horellou, C. 2011, *A&A*, 527, A117
- Kim, S., Wardlow, J. L., Cooray, A., et al. 2012, *ApJ*, 756, 28
- Knudsen, K. K., van der Werf, P. P., & Kneib, J.-P. 2008, *MNRAS*, 384, 1611
- Kohno, K., Yamaguchi, Y., Tamura, Y., et al. 2016, in *IAU Symposium*, Vol. 319, *Galaxies at High Redshift and Their Evolution Over Cosmic Time*, ed. S. Kaviraj, 92–95
- Labbé, I., Huang, J., Franx, M., et al. 2005, *ApJL*, 624, L81
- Lagache, G., Puget, J.-L., & Dole, H. 2005, *ARA&A*, 43, 727
- Lang, D., Hogg, D. W., & Schlegel, D. J. 2016, *AJ*, 151, 36
- Laporte, N., Bauer, F. E., Troncoso-Iribarren, P., et al. 2017, *A&A*, 604, A132
- Laurent, G. T., Aguirre, J. E., Glenn, J., et al. 2005, *ApJ*, 623, 742
- Lawrence, A., Warren, S. J., Almaini, O., et al. 2007, *MNRAS*, 379, 1599
- Lonsdale, C., Polletta, M. d. C., Surace, J., et al. 2004, *ApJS*, 154, 54
- Mauduit, J.-C., Lacy, M., Farrah, D., et al. 2012, *PASP*, 124, 714
- McMullin, J. P., Waters, B., Schiebel, D., Young, W., & Golap, K. 2007, in *Astronomical Society of the Pacific Conference Series*, Vol. 376, *Astronomical Data Analysis Software and Systems XVI*, ed. R. A. Shaw, F. Hill, & D. J. Bell, 127
- Michałowski, M. J., Dunlop, J. S., Koprowski, M. P., et al. 2017, *MNRAS*, 469, 492
- Miettinen, O., Novak, M., Smolčić, V., et al. 2015, *A&A*, 584, A32
- Mohan, N., & Rafferty, D. 2015, *PyBDSF: Python Blob Detection and Source Finder*, *Astrophysics Source Code Library*, , , ascl:1502.007
- Nyland, K., Lacy, M., Sajina, A., et al. 2017, *ApJS*, 230, 9
- Ono, Y., Ouchi, M., Kurono, Y., & Momose, R. 2014, *ApJ*, 795, 5
- Oteo, I., Zwaan, M. A., Iverson, R. J., Smail, I., & Biggs, A. D. 2016, *ApJ*, 822, 36
- Ouchi, M., Ellis, R., Ono, Y., et al. 2013, *ApJ*, 778, 102
- Patel, S. G., Kelson, D. D., Holden, B. P., Franx, M., & Illingworth, G. D. 2011, *ApJ*, 735, 53
- Pentericci, L., Carniani, S., Castellano, M., et al. 2016, *ApJL*, 829, L11
- Perera, T. A., Chapin, E. L., Austermann, J. E., et al. 2008, *MNRAS*, 391, 1227
- Pope, A., Scott, D., Dickinson, M., et al. 2006, *MNRAS*, 370, 1185
- Rowan-Robinson, M., Gonzalez-Solares, E., Vaccari, M., & Marchetti, L. 2013, *MNRAS*, 428, 1958
- Rowan-Robinson, M., Babbedge, T., Oliver, S., et al. 2008, *MNRAS*, 386, 697
- Scott, K. S., Yun, M. S., Wilson, G. W., et al. 2010, *MNRAS*, 405, 2260
- Scott, K. S., Wilson, G. W., Aretxaga, I., et al. 2012, *MNRAS*, 423, 575
- Sekiguchi, K., & SXDS Team. 2004, in *Bulletin of the American Astronomical Society*, Vol. 36, *American Astronomical Society Meeting Abstracts*, 1478
- Seko, A., Ohta, K., Yabe, K., et al. 2016a, *ApJ*, 819, 82
- , 2016b, *ApJ*, 833, 53
- Simpson, J. M., Swinbank, A. M., Smail, I., et al. 2014, *ApJ*, 788, 125
- Simpson, J. M., Smail, I., Swinbank, A. M., et al. 2017, *ApJ*, 839, 58
- Siringo, G., Kreysa, E., Kovács, A., et al. 2009, *A&A*, 497, 945
- Smail, I., Iverson, R. J., & Blain, A. W. 1997, *ApJL*, 490, L5
- Smail, I., Iverson, R. J., Blain, A. W., & Kneib, J.-P. 2002, *MNRAS*, 331, 495
- Smith, D. J. B., Dunne, L., Maddox, S. J., et al. 2011, *MNRAS*, 416, 857
- Steidel, C. C., Giavalisco, M., Pettini, M., Dickinson, M., & Adelberger, K. L. 1996, *ApJL*, 462, L17
- Swinbank, A. M., Simpson, J. M., Smail, I., et al. 2014, *MNRAS*, 438, 1267
- Tokunaga, A. T., Simons, D. A., & Vacca, W. D. 2002, *PASP*, 114, 180
- Viero, M. P., Moncelsi, L., Quadri, R. F., et al. 2013, *ApJ*, 779, 32
- Wardlow, J. L., Smail, I., Coppin, K. E. K., et al. 2011, *MNRAS*, 415, 1479
- Weiß, A., Kovács, A., Coppin, K., et al. 2009, *ApJ*, 707, 1201
- Whitaker, K. E., Labbé, I., van Dokkum, P. G., et al. 2011, *ApJ*, 735, 86
- Williams, R. J., Quadri, R. F., Franx, M., van Dokkum, P., & Labbé, I. 2009, *ApJ*, 691, 1879
- Willott, C. J., Carilli, C. L., Wagg, J., & Wang, R. 2015, *ApJ*, 807, 180
- Willott, C. J., McLure, R. J., Hibon, P., et al. 2013, *AJ*, 145, 4
- Wuyts, S., Labbé, I., Franx, M., et al. 2007, *ApJ*, 655, 51
- Yamaguchi, Y., Tamura, Y., Kohno, K., et al. 2016, *PASJ*, 68, 82